Advancing Optical Sensing and Device Integration in Multi-Core Fibers

Tesis
entregada a la
Universidad de Chile
en cumplimiento parcial de los requisitos
para optar al grado de
Magíster en Ciencias Físicas
Facultad de Ciencias

por

Víctor Alejandro Muñoz Mosqueira

Diciembre, 2024

Directores de Tesis: **Dra. Carla Hermann**
Dr. Stephen Walborn

FACULTAD DE CIENCIAS

UNIVERSIDAD DE CHILE

INFORME DE APROBACIÓN

TESIS DE MAGÍSTER

Se informa a la Escuela de Postgrado de la Facultad de Ciencias que la Tesis de Magíster presentada por el candidato

Víctor Alejandro Muñoz Mosqueira

ha sido aprobada por la Comisión de Evaluación de la Tesis como requisito para optar al grado de Magíster en Ciencias Físicas, en el examen de Defensa de Tesis rendido el día 07 de Enero de 2025.

Directores de Tesis

Dra. Carla Hermann ______________________

Dr. Stephen Walborn ______________________

Comisión de Evaluación de la Tesis

Dra. Carla Hermann ______________________

Dr. Stephen Walborn ______________________

Dr. Pablo Solano ______________________

Dr. Marcel Clerc (Presidente) ______________________

Le dedico esta tesis a mi abuela. En su día tome el magíster para poder cuidarla un poco mejor al final de su vida, finalmente falleció durante mi magíster.

No me arrepiento.

BIOGRAFÍA

Nací, me gustó la física, la elegí de profesión, y ahora soy casi magíster.

Éso por ahora.

AGRADECIMIENTOS

Agradezco a mi papá por inculcarme la física y la matemática desde pequeño, intencional o no.

También agradezco a Eiichiro Oda por su dedicación a One Piece, ha sido un apoyo desde mis inicios.

Y finalmente, agradezco a Paloma y Römi, por el gran apoyo y alegría en momentos de crisis.

...

Esta investigación ha sido apoyada financieramente por FONDECYT REGULAR grant N° 1230897, ANID - Millenium Science Inititive Program - ICN17_012. A.D., y el Millenium Institute for Research in Optics.

Index

List of Figures

Abbreviations and Units

SDM	Space-Division Multiplexing
MCF	Multi-Core Fiber
SMF	Single-Mode Fiber
MZI	Mach-Zehnder Interferometer
SQL	Standard Quantum Limit
BS	Beam Splitter
MBS	Multi-Port Beam Splitter
PBS	Polarizing Beam Splitter
PC	Polarization Controller
IPC	Inline Polarization Controller
QFT	Quantum Fourier Transform
DFT	Discrete Fourier Transform
QKD	Quantum Key Distribution
EMF	Electromagnetic Field
SG	Susskind-Glogower
BCH	Baker-Campbell-Hausdorff
DM	Demultiplexer
QWP	Quarter-Wave Plate
HWP	Half-Wave Plate
FBG	Fiber Bragg Gratings
SI	Sistema Internacional
dB	Decibel
nm	Nanometer

RESUMEN

Esta tesis explora la integración de recursos cuánticos en sistemas interférometricos basados en fibras de multinúcleo para mejorar las capacidades de medición de precisión y múltiples parámetros. Utilizando divisores de haz multi-puerto, investigamos analíticamente la propagación de estados cuánticos y su impacto en el rendimiento metrológico y computacional. Estudios analíticos y numéricos de interferómetros de Mach-Zehnder revelan configuraciones que optimizan la eficiencia, precisión y/o robustez para la estimación de parámetros tanto individuales como múltiples. Además, se presenta una caracterización experimental preliminar de un controlador de polarización inline en fibras multinúcleo, ofreciendo el potencial para mejorar la calidad de la interferencia y para futuras aplicaciones en comunicaciones cuánticas. Estos hallazgos sientan las bases para el avance de las tecnologías cuánticas basadas en fibras multinúcleo, con potenciales aplicaciones en sensores, comunicación y computación.

ABSTRACT

This thesis explores the integration of quantum resources into multi-core fiber-based interferometric systems to enhance precision and multi-parameter measurement capabilities. Using multi-port beam splitters, we analytically investigate the propagation of quantum states and their impact on metrological and computational performances. Analytical and numerical studies of multi-port Mach-Zehnder interferometers reveal configurations that optimize efficiency, precision and/or robustness for both single- and multi-parameter estimation. Additionally, a preliminary experimental characterization of an inline polarization controller in multi-core fibers is presented, offering potential for improved interference quality and future quantum communication applications. These findings lay the foundation for advancing multi-core fiber-based quantum technologies, with potential applications in sensing, communication, and computation.

Chapter 1

Introduction

1.1. Background and Motivation

The demand for enhanced information transmission and precision measurement has driven the development of advanced optical and quantum technologies. Yet, some of this technologies face significant challenges. For instance, standard single-mode fibers (SMFs), which dominate the field, are limited by their capacity to support only a single spatial mode, leading to saturation in data transmission rates and reduced efficiency. In this context, space-division multiplexing (SDM) represents a solution to current limitations by enabling increased data transmission in available devices [2]. Among these, multi-core fibers (MCFs) [3,4] have emerged as a promising candidate due to their ability to support multiple independent spatial modes, compactness, and stability. These fibers not only address the capacity limitations of standard SMFs, but also open pathways for integrating sensing, communication, and computational technologies.

In parallel, interferometers, such as Mach-Zehnder interferometers (MZIs) [5] or Michelson interferometers [6], play a pivotal role in optical systems for precision measurement. These devices extract information of a phenomenon that produces a change in propagating light from the resulting interference pattern. Integrating interferometric systems into optical fibers brings numerous advantages, such as enhanced stability and spatial freedom. Phenomena like temperature changes, torsions, imperfections, voltages, etc., produce variations in fiber length or refractive index. These variations are detectable from the interference patterns with high precision by several methods [7–10].

Moreover, MCFs enable a powerful combination of SDM and interferometric systems. By assigning individual cores to interferometric arms, MCFs facilitate compact and robust setups. Additionally, due to the cores being displaced from the fiber's center, MCFs offer enhanced precision in response to external perturbations, such as flexion, tension, curvature [8, 11], vibration [12, 13], torsion [14, 15], fluid flux [11, 16], etc. Interferometric sensors implemented in MCFs have enabled the development of highly precise measurements of environmental factors like temperature [17, 18], gas concentration [19], refractive index [20, 21], etc. Further exploring MCF-based interferometers will lead to strong metrological applications.

Despite the remarkable capabilities of MCF-based interferometers, as in any physical system, their precision is fundamentally constrained by the Heisenberg uncertainty principle. This principle states states that there is a limit to which a pair of conjugate physical quantities can be simultaneously known. When using only classical states (coherent light), the precision achievable is bounded by the standard quantum limit (SQL) [22]. It states that the uncertainty achievable in a measurement scales as $\frac{1}{\sqrt{N}}$, where N is the photon number in the system (or energy in the system). This is the precision limitation in classical metrology.

However, using inherently quantum states provides a pathway to surpass the SQL by redistributing uncertainties and thus exploiting the Heisenberg uncertainty principle. For example, squeezed states achieve enhanced precision in one variable at the expense of increased uncertainty in its conjugate variable. For squeezed states, the precision scales as $\frac{e^{-r}}{\sqrt{N}}$, where r is the squeezing parameter. Furthermore, when using Fock states, the uncertainty scales as $\frac{1}{N}$. This is known as the Heisenberg limit [22], an unbreakable precision limit that emerges directly from the Heisenberg uncertainty principle. Leveraging these advantages, interferometers serve as crucial tools in quantum metrology, enabling significant uncertainty reduction.

To construct advanced interferometers, a deep understanding of beam splitters (BSs) is essential. For SDM purposes in MCFs, this requires the use of multi-port beam splitters (MBSs). These devices are not only critical components for routing and manipulating light but also hold significant applications in quantum state engineering [23–25] and quantum information through the application of unitary transformations [1]. Therefore, the propagation of quantum states and the implementation of MBSs in MCFs are crucial for the outcomes of this thesis.

Additionally, orthogonal polarizations propagated along the arms of the interferometer do not interfere, so in order to successfully make interference-based processes, some control over the polarization is required. Changes and/or fluctuations in light polarization lead to several errors in potential measurements [26–28]. In this thesis, one of the focuses is placed on the inline polarization controller (IPC), a device capable of controlling the polarization directly within the fiber through stress-induced birefringence. Its action is well known for a SMF. However, for a MCF, characterization of the IPC has not yet been documented in the literature. Achieving this characterization will lead to polarization control over multiple signals simultaneously, providing applications for quantum metrology, by allowing effective interference, and quantum communications, since information can be encoded in the state of polarization.

The general objective of this thesis is to advance the development of precision optical sensors integrated into MCFs, by leveraging on quantum resources to achieve enhanced precision, characterizing propagation through MBSs, and enabling polarization control in MCFs. Since the later is needed to some extent to experimentally realize interferometry, this thesis consists of theoretical work regarding MBSs and MZIs, done in the meantime of an experimental work, regarding polarization control in MCFs. Specifically, this thesis seeks to analytically and numerically explore a multi-port MZI, focusing on enhancing precision with classical and quantum resources (coherent and squeezed states). To achieve this, we explore possible parameterizations, configurations for the input state, and measurable operators. We found favorable scenarios for single- and multi-parameter estimation with enhanced and/or robust uncertainties, comparable with the standard 2-port interferometer. Additionally, we analytically study the implementation of MBSs in MCFs by modeling them as coupled waveguide arrays (approach that comes from their experimental implementation [1]), focusing on their potential to manipulate quantum states and perform unitary transformations. The results propose a perspective for studying squeezing dynamics in such system from conserved quantities, and highlight MBSs integrated into MCFs as a viable device to implement any balanced unitary transformation, particularly a Fourier transform. Finally, this thesis aims to experimentally characterize the transformation of the IPC on each core of a 4-core MCF, enabling effective interference and communications systems. A toy model to characterize these transformations based on the SMF transformation is proposed, with results that could later lead to a more accurate model. However, enough data to use quantum process tomography has already been gathered. We will proceed with this in the near future.

The findings presented in this thesis are not only fundamental for advancing the precision and functionality of MCF-based systems but also promise for real-world applications in sensing, communication, and quantum information processing. By addressing critical challenges—such as enhanced precision through quantum resources, effective beam splitter implementations, and polarization control—this work paves the way for the practical integration of MCF-based technologies into advanced metrological and computational systems. The potential applications of these developments are discussed in detail in the following section, highlighting their impact on both quantum and classical optical technologies.

1.2. Potential Application Contexts

In this Section, we provide examples of context where the work presented in this thesis may be applicable.

1.2.1. Quantum Metrology

Quantum metrology leverages quantum phenomena—particularly squeezing and entanglement—to measure physical parameters with precision surpassing classical limits [29–31]. In this field, optical interferometers are devices with innumerable metrological applications. In essence, any physical phenomenon that produces a change in the propagation of light, in particular to the phase front, can be measured with an interferometer. Form a quantum metrology perspective, interferometers can fully exploit the nonclassical nature of light, since quantum states of optical modes can be used as input to the device, resulting in improved precision [32, 33].

The results presented in this work related to multiparameter estimation with reduced and/or robust uncertainty, have direct implications for quantum metrology. These applications are further detailed in Chapter 5.

1.2.2. Quantum Information Processing

Quantum information refers to the description of the state of a quantum system. Quantum information processing involves utilizing this information for purposes such as quantum cryptography, characterizing quantum transformations, and developing quantum algorithms that enhance computational efficiency [34]. Photonic quantum computing has beed considered for more than twenty years as a viable candidate for a fault-tolerant quantum computer [35]. Currently, one of the largest quantum computing companies, PsiQuantum, is pursuing this route.

In particular, the capability to perform a quantum fourier transform (QFT) is highly valuable. The QFT is known for its ability to accelerate certain computations compared to other unitary transformations [36, 37].

Relevant results for this field, including squeezed state propagation and the implementation of the QFT, are presented in Chapters 4 and 6.

1.2.3. Quantum Communication and Cryptography

Quantum communication involves the transfer of quantum information over a distance, with a focus on ensuring secure, robust, and efficient communication. This field encompasses technologies like quantum key distribution (QKD), which uses principles of quantum mechanics to enable unbreakable encryption.

The multi-core fibers studied as part of this thesis are an example of space division multiplexing technology, which is a candidate to resolve the capacity crunch in current classical telecommunications [2]. The MCF interferometers could play an important role in fast switching and routing in both classical and quantum networks.

The results in this thesis involving precise interferometric measurements and polarization manipulation, hold promise for applications in quantum communication and cryptography, as discussed in Chapters 5 and 6.

Chapter 2

Theoretical Framework

This chapter presents the fundamental mathematical concepts underlying this work. We begin in Section 2.1 by reviewing the classical electromagnetic description of light propagation. Subsequently, in Section 2.2, we transition to a quantum mechanical perspective, necessitated by the quantization of light, and examine the most relevant states of light for our investigation. Section 3.1 examines the 2×2 Mach-Zehnder interferometer and its significance in measuring phase shifts in propagating light. Section 3.2.1 introduces multi-port beam splitters, which serve as building blocks for the multi-port MZI. In Section 3.3, we propose a method for controlling polarization in a MCF using an in-line polarization controller. Finally, Section 1.2 explores potential applications of our research.

2.1. Classical Light

Light, classically described, is an electromagnetic wave, governed by Maxwell's equations (in SI units):

$$
\begin{aligned}
\vec{\nabla} \cdot \vec{E} = \frac{\rho}{\varepsilon_0}\,, \qquad & \vec{\nabla} \cdot \vec{B} = 0\,, \\
\vec{\nabla} \times \vec{E} = -\frac{\partial \vec{B}}{\partial t}\,, \quad & \vec{\nabla} \times \vec{B} = \mu_0 \left(\vec{J} + \varepsilon_0 \frac{\partial \vec{E}}{\partial t} \right)\,.
\end{aligned} \tag{2.1}
$$

In the absence of charges (vacuum), $\rho = 0$ and $\vec{J} = 0$. We can express $\vec{E}$ and $\vec{B}$ in terms of a vector potential $\vec{A}$:

$$
\begin{aligned}
\vec{B} &= \vec{\nabla} \times \vec{A}\,, \\
\vec{E} &= -\frac{\partial \vec{A}}{\partial t}\,.
\end{aligned} \tag{2.2}
$$

Eq. (2.2) holds considering the Coulomb Gauge ($\vec{\nabla} \cdot \vec{A} = 0$), which ensures that $\vec{A}$ is a transverse field with only two components. Since we are considering free light propagation with no relativistic effects, this gauge choice suffices our need for degrees of freedom. It is worth noting that choosing the Coulomb gauge over, e.g. the Lorenz gauge, is not strictly necessary as the results in eqs. (2.10) would remain unchanged [38]. However, the standard procedure in the community is using the Coulomb gauge. For further discussion one may like to read quantum field theory or quantum electrodynamics texts.

Substituting Eqs. (2.2) into Ampere's law from Eq. (2.1), we obtain

$$
\nabla^2 \vec{A} = \frac{1}{c^2} \frac{\partial^2 \vec{A}}{\partial t^2}\,, \tag{2.3}
$$

which is a wave equation for the vector potential. Expanding $\vec{A}$ in its normal modes of vibration in, say, a volume $V = L^3$, results in

$$
\vec{A}(\vec{r}, t) = \sum_k \sum_{\alpha=1}^{2} \left(C_k a_{k,\alpha}(t) \vec{u}_{k,\alpha}(\vec{r}) + c.c. \right)\,, \tag{2.4}
$$

where $a_{k,\alpha}$ is a time dependent amplitude, $\vec{u}_{k,\alpha}$ is the position dependent polarization vector, and $C_k = \sqrt{\frac{\hbar}{2\varepsilon_0\omega_k}}$ are normalization constants. Here, the wave number k represents the normal mode, and α the polarization component of the k-th mode. Replacing Eq. (2.4) into Eq. (2.3) and equating terms we get

$$a_{k,\alpha}\nabla^2\vec{u}_{k,\alpha} = \frac{1}{c^2}\frac{\partial^2 a_{k,\alpha}}{\partial t^2}\vec{u}_{k,\alpha}\,. \tag{2.5}$$

We now write the vectorial part as $\vec{u}_{k,\alpha}(\vec{r}) = u_{k,\alpha}(\vec{r})\hat{\varepsilon}_{k,\alpha}$ such that by separation of variables Eq. (2.5) becomes

$$\frac{\nabla^2 u_{k,\alpha}}{u_{k,\alpha}} = \frac{1}{c^2 a_{k,\alpha}}\frac{\partial^2 a_{k,\alpha}}{\partial t^2} = -k^2\,, \tag{2.6}$$

with $-k^2$ being the separation constant for each normal mode. From Eq. (2.6) we arrive to

$$\begin{aligned} \nabla^2 u_{k,\alpha} + k^2 u_{k,\alpha} &= 0\,, \\ \frac{\partial^2 a_{k,\alpha}}{\partial t^2} + \omega_k^2 a_{k,\alpha} &= 0\,, \end{aligned} \tag{2.7}$$

where $\omega_k = ck$. From Eqs. (2.7) we note that both $a_{k,\alpha}$ and $u_{k,\alpha}$ are sinusoidal or exponential, so we are expanding $\vec{A}$ as a superposition of harmonic oscillators. For periodic boundary conditions one have the solutions

$$\begin{aligned} \vec{u}_{k,\alpha}(\vec{r}) &= \frac{e^{i\vec{k}\cdot\vec{r}}}{\sqrt{V}}\vec{\varepsilon}_{k,\alpha}\,, \\ a_{k,\alpha}(t) &= a_{k,\alpha}e^{-i\omega_k t}\,, \end{aligned} \tag{2.8}$$

with real $\vec{\varepsilon}_{k,\alpha}$ and complex $a_{k,\alpha}$. Replacing Eq. (2.8) in Eq. (2.4) we obtain the vector potential:

$$\vec{A} = \sum_k \sum_{\alpha=1}^{2} \sqrt{\frac{\hbar}{2\varepsilon_0\omega_k V}}\left(a_{k,\alpha}e^{i(\vec{k}\cdot\vec{r}-\omega_k t)} + c.c.\right)\hat{\varepsilon}_{k,\alpha}\,. \tag{2.9}$$

Here, $\vec{k} = \frac{2\pi}{L}(n_x, n_y, n_z)$ and $\varepsilon_{k,\alpha}$ are the wave and polarization vectors respectively, and n_ℓ are integers. Since we are using the Coulomb Gauge, these vectors satisfy $\vec{k} \cdot \hat{\varepsilon}_{k,\alpha} = 0$. Also, the polarization vector can be orthonormal by construction, such that $\hat{\varepsilon}_{k,\alpha} \cdot \hat{\varepsilon}_{k,\alpha'} = \delta_{\alpha\alpha'}$. Using Eq. (2.9) in Eqs. (2.2) we find the electric and magnetic fields,

$$
\begin{aligned}
\vec{E}(\vec{r}, t) &= i \sum_k \sum_{\alpha=1}^{2} \mathcal{E}_k \left(a_{k,\alpha} e^{i(\vec{k}\cdot\vec{r} - \omega_k t)} - c.c. \right) \hat{\varepsilon}_{k,\alpha} \\
\vec{B}(\vec{r}, t) &= i \sum_k \sum_{\alpha=1}^{2} \frac{\mathcal{E}_k}{\omega_{k,\alpha}} \left(a_{k,\alpha} e^{i(\vec{k}\cdot\vec{r} - \omega_k t)} - c.c. \right) \vec{k} \times \hat{\varepsilon}_{k,\alpha} \, ,
\end{aligned}
\tag{2.10}
$$

where $\mathcal{E}_k = \sqrt{\frac{\hbar\omega_k}{2\varepsilon_0 V}}$ is the electric field amplitude due to one photon in the mode k, as we will see in the following section. Now that we found $\vec{E}$ and $\vec{B}$, we can develop the Hamiltonian, obtaining

$$
\begin{aligned}
H &= \frac{\varepsilon_0}{2} \int_V \left(|\vec{E}|^2 + c^2 |\vec{B}|^2 \right) d^3 r \\
&= \frac{1}{2} \sum_k \sum_{\alpha=1}^{2} \hbar\omega_k (a_{k,\alpha} a^*_{k,\alpha} + a^*_{k,\alpha} a_{k,\alpha}) \, .
\end{aligned}
\tag{2.11}
$$

If we make the change

$$
\begin{aligned}
a_{k,\alpha} &= \frac{1}{\sqrt{2\hbar\omega_k}} \left(\omega_k q_{k,\alpha} + i p_{k,\alpha} \right) \, , \\
a^*_{k,\alpha} &= \frac{1}{\sqrt{2\hbar\omega_k}} \left(\omega_k q_{k,\alpha} - i p_{k,\alpha} \right) \, ,
\end{aligned}
\tag{2.12}
$$

then Eq. (2.11) becomes

$$
H = \frac{1}{2} \sum_k \sum_{\alpha=1}^{2} \left(p^2_{k,\alpha} + \omega_k^2 q^2_{k,\alpha} \right) \, , \tag{2.13}
$$

which is the typical Hamiltonian for a harmonic oscillator in classical mechanics, with $q_{k,\alpha}$ and $p_{k,\alpha}$ representing the positions and momenta, respectively. This result indicates that the total energy is given by the direct sum of all the parts in the system, and if the system is empty, it equals zero, as expected.

2.2. Nonclassical Light

In this section, we review the main consequences of quantizing the electromagnetic field (EMF), including the emergence of new states of light, the differences between these states and classical light, and the distinctions among the states themselves. Special emphasis is placed on the expectation values and uncertainties of their quadratures. These expectations and uncertainties are the foundation for Chapter 5.

2.2.1. Quantization of the Electromagnetic Field

To quantize the EMF, we promote the positions and momenta from coordinates to operators, such that

$$[\hat{q}_{k,\alpha}, \hat{p}_{k',\alpha'}] = \delta_{k,k'}\delta_{\alpha,\alpha'} i\hbar \hat{I} \,, \tag{2.14}$$

indicating that for a given mode and polarization, these operators no longer commute, differing by a very small quantity ($\hbar = 1.05 \times 10^{-34}$ Js). This change also promotes the complex amplitudes of the potential vector to operators, as seen in Eq. (2.12). Thus, now we have

$$\begin{aligned} \hat{a}_{k,\alpha} &= \frac{1}{\sqrt{2\hbar\omega_k}} \left(\omega_k \hat{q}_{k,\alpha} + i\hat{p}_{k,\alpha}\right) \,, \\ \hat{a}^{\dagger}_{k,\alpha} &= \frac{1}{\sqrt{2\hbar\omega_k}} \left(\omega_k \hat{q}_{k,\alpha} - i\hat{p}_{k,\alpha}\right) \,. \end{aligned} \tag{2.15}$$

Here, $\hat{a}_{k,\alpha}$ and $\hat{a}^{\dagger}{}_{k,\alpha}$ are called the annihilation and creation operators respectively (or ladder operators), for reasons that will become clear in section 2.2.4. By combining Eq. (2.14) and Eq. (2.15), we arrive at

$$
\begin{aligned}
&[\hat{a}_{k,\alpha}, \hat{a}^{\dagger}_{k',\alpha'}] = \delta_{k,k'}\delta_{\alpha,\alpha'}\hat{I} \, , \\
&[\hat{a}_{k,\alpha}, \hat{a}_{k',\alpha'}] = 0 \, .
\end{aligned}
\tag{2.16}
$$

After promoting the variables to operators, the electric field in Eq. (2.10) becomes the operator

$$
\hat{E} = i \sum_k \sum_{\alpha=1}^{2} \mathcal{E}_k \left(\hat{a}_{k,\alpha} e^{i\varphi} - \hat{a}^{\dagger}_{k,\alpha} e^{-i\varphi} \right) \, , \tag{2.17}
$$

where $\varphi = \vec{k} \cdot \vec{r} - \omega_k t$ is the phase due to propagation. Likewise, using the commutation rules in Eq. (2.16), we can rewrite the classical Hamiltonian in Eq. (2.11) in its operator form as

$$
\hat{H} = \sum_k \sum_{\alpha=1}^{2} \hbar\omega_k \left(\hat{a}^{\dagger}_{k,\alpha} \hat{a}_{k,\alpha} + \frac{1}{2}\hat{I} \right) \, . \tag{2.18}
$$

In essence, this is similar to Eq. (2.11), as it still is the direct sum of every mode in the system. However, there is a fundamental difference: the vacuum energy. The Hamiltonian in Eq. (2.18) adds a base energy for every term (even for the vacuum), causing the energy to diverge when considering infinite modes. To address this, we interpret this term as a zero-energy displacement with no physical consequences. For a deeper treatment, we recommend consulting quantum field theory texts, as this falls outside the scope of this thesis.

2.2.2. Polarization of Quantum Light

Polarization refers to the spatial components of the propagated field, similar to how normal modes refer to the frequency components. It is a relevant concept since light with independent polarizations does not interfere. In a classical description, polarizations are the directions in which the field oscillates. Generally, these directions can be arbitrary, but for transverse propagation, the polarizations are restricted to the transverse plane perpendicular to the propagation direction. Since the polarizations exist in a 2-D space, there can be up to two independent (orthonormal) polarizations at a time, forming a basis for the polarizations.

In a quantum framework, we describe light as being in a specific polarization state, although the concept of polarization remains the same. The principal polarization bases are illustrated Fig. 2.1.

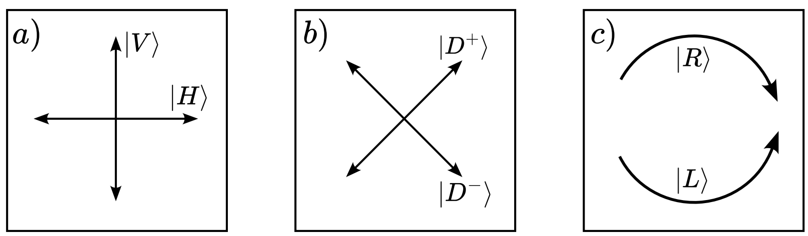

Fig. 2.1: Representation of the principal polarization bases. The arrows represent the directions of intensity oscillations at the wave front. a) Standard basis. b) Hadamard Basis. c) Fourier Basis.

The polarizations states in Fig. 2.1 are related by the following relations:

$$\begin{aligned} |D^+\rangle &= \frac{|H\rangle + |V\rangle}{\sqrt{2}}\,, \\ |D^-\rangle &= \frac{|H\rangle - |V\rangle}{\sqrt{2}}\,, \\ |R\rangle &= \frac{|H\rangle + i|V\rangle}{\sqrt{2}}\,, \\ |L\rangle &= \frac{|H\rangle - i|V\rangle}{\sqrt{2}}\,. \end{aligned} \tag{2.19}$$

As seen from Fig. 2.1, polarizations can be classified as linear or circular, depending on their distribution in the transverse plane. Circular polarizations do not have a well-defined linear polarization associated with them. This can be understood by noting that $|R\rangle$ and $|L\rangle$ are obtained when $|V\rangle$ is phase-shifted by $\pm\frac{\pi}{2}$ relative to $|H\rangle$. This phase shift can result from various effects (e.g., different propagation velocities for each polarization), causing the light to lack a predominant linear polarization. Other phase shifts lead to elliptical polarizations. In our experiment (Chapter 6), the required basis polarizations are generated using a quarter'wave plate to induce these phase shifts.

When working with polarization, the Stokes or Bloch parameters are useful tools for visualizing and characterizing polarization[1]. Both of these parameters represent the intensity of light in the bases defined in Fig. 2.1. Stokes parameters are used in a classical context, for partially and fully polarized light, while Bloch parameters are used in a quantum context, for pure and mixed states. Here, we will use the latter. Bloch parameters a_1, a_2, and a_3 are mapped onto the Bloch sphere in Fig. 2.2. Points on the sphere's surface represent pure states, while points inside the sphere correspond to mixed states.

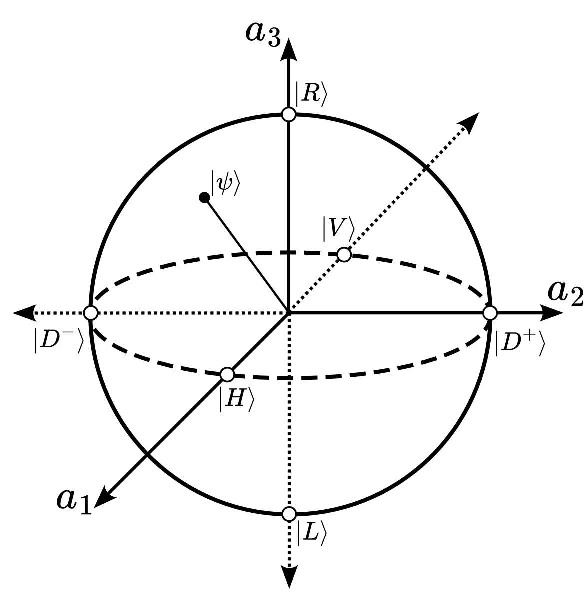

[1]In fact, they are a useful representation for any qubit state, including polarization.

Fig. 2.2: Bloch sphere representation of an arbitrary state $|\psi\rangle$. Each axis correspond to a Bloch parameter, wich are associated to a certain basis.

For the analytic expressions of Bloch parameters, we can note that the basis states in Fig. 2.1 are eigenstates of the Pauli matrices. Consequently, for any state, its density matrix can be expressed using the Bloch parameters a_i as

$$\begin{aligned}\rho &= \frac{1}{2}\left(\hat{I} + a_1\sigma_z + a_2\sigma_x + a_3\sigma_y\right) \\ &= \frac{1}{2}\left(\hat{I} + \vec{a}\cdot\vec{\sigma}\right) ,\end{aligned} \tag{2.20}$$

where σ_i are the Pauli matrices and $\vec{a} = (a_1, a_2, a_2)$ is the Bloch vector. Solving for a_i, we find

$$\begin{aligned}a_1 &= \langle H|\rho|H\rangle - \langle V|\rho|V\rangle = \rho_{11} - \rho_{22} , \\ a_2 &= \langle +|\rho|+\rangle - \langle -|\rho|-\rangle = 2\Re(\rho_{12}) , \\ a_3 &= \langle R|\rho|R\rangle - \langle L|\rho|L\rangle = 2\Im(\rho_{21}) .\end{aligned} \tag{2.21}$$

For a pure state, we can write

$$|\psi\rangle = p_h|H\rangle + p_v|V\rangle , \tag{2.22}$$

and the Bloch parameters become

$$\begin{aligned}a_1 &= |p_h|^2 - |p_v|^2 , \\ a_2 &= 2\Re\left(p_h p_v^*\right) , \\ a_3 &= 2\Im\left(p_h^* p_v\right) .\end{aligned} \tag{2.23}$$

If the state is normalized, we can define phases θ, φ_h, and φ_v such that $p_h = \cos\left(\frac{\theta}{2}\right) e^{i\varphi_h}$ and $p_v = \sin\left(\frac{\theta}{2}\right) e^{i\varphi_v}$. Then, the Bloch parameters become

$$
\begin{aligned}
a_1 &= \cos\theta\,, \\
a_2 &= \sin\theta\cos\Delta_{vh}\,, \\
a_3 &= \sin\theta\sin\Delta_{vh}\,,
\end{aligned}
\tag{2.24}
$$

where $\Delta_{vh} = \varphi_v - \varphi_h$. The expressions in Eq. (2.24) resemble spherical coordinates, where θ and Δ_{vh} are the polar and azimuthal angles, respectively, although here the north pole corresponds to $a_1 = 1$.

2.2.3. Quadratures and uncertainty

A useful concept for the study of quantum light are the quadratures. We often make diagrams in the phase space (e.g., the Wigner function), using the position and momentum. Here we define the quadratures, which are analogous but differ only in units, with the quadratures being dimensionless. The quadrature operators for a single mode and polarization field (for simplicity of notation) are defined as

$$
\begin{aligned}
\hat{X}_1 &= \sqrt{\frac{\omega}{2\hbar}}\hat{q} = \frac{\hat{a}+\hat{a}^\dagger}{2}\,, \\
\hat{X}_2 &= \frac{1}{\sqrt{2\hbar\omega}}\hat{p} = \frac{\hat{a}-\hat{a}^\dagger}{2i}\,,
\end{aligned}
\tag{2.25}
$$

and they represent the real and imaginary part of the complex amplitude defined by $\hat{a}$, as we can see from their expression. We can actually define a general quadrature as

$$
\hat{X}(\nu) = \frac{\hat{a}e^{-i\nu} + \hat{a}^\dagger e^{i\nu}}{2}\,, \tag{2.26}
$$

which can be interpreted as a continuous rotation in phase space. This recovers $\hat{X}_1$ and $\hat{X}_2$ for $\nu = 0, \frac{\pi}{2}$, respectively, making it clearer that $\hat{X}_1$ and $\hat{X}_2$ are, in fact, in quadrature. The commutation relation between two quadratures shifted by $\frac{\pi}{2}$ is

$$\left[\hat{X}(\nu), \hat{X}\left(\nu + \frac{\pi}{2}\right)\right] = \frac{i}{2}\,. \tag{2.27}$$

Another useful expression comes from developing the electric field operator using these quadratures. In order to do this, we first promote the complex amplitudes in Eq. (2.10) to operators and then substitute Eq. (2.25) into it. For simplicity, we do this for a single-mode field, arriving at

$$\hat{E} = -2\mathcal{E}_0\left(\hat{X}_1 \sin\varphi + \hat{X}_2 \cos\varphi\right)\,. \tag{2.28}$$

From Eq. (2.28), it is even more explicit that the quadratures are associated with the amplitudes in quadrature.

Lastly, to represent a quantum state in the quadrature space, we can make a phase space diagram defined by the quadratures. In such diagrams, each point in the space corresponds to the expectation values of the quadratures, but we also depict an error area, corresponding to the fluctuations in each quadrature. If we consider a state $|\psi\rangle$, we need to compute $\langle\psi|\hat{X}(\nu)|\psi\rangle$, and its fluctuations:

$$\Delta\left\langle \hat{X}(\nu)\right\rangle = \sqrt{\langle\psi|\hat{X}^2(\nu)|\psi\rangle - \langle\psi|\hat{X}(\nu)|\psi\rangle^2}\,, \tag{2.29}$$

evaluating ν to consider any pair of quadratures we may want to work with.[2] The squared quadrature is

$$\hat{X}^2(\nu) = \frac{1}{4}\left(1 + 2\hat{a}^\dagger\hat{a} + \hat{a}^2 e^{-2i\nu} + \hat{a}^{\dagger\,2} e^{2i\nu}\right)\,, \tag{2.30}$$

[2]Of course, this is the procedure for any operator, not just the quadratures.

which for $\nu = 0, \frac{\pi}{2}$ reduces to

$$\begin{aligned} \hat{X}_1^2 &= \frac{1}{4}\left(1 + 2\hat{a}^\dagger\hat{a} + \hat{a}^2 + \hat{a}^{\dagger\,2}\right) \,, \\ \hat{X}_2^2 &= \frac{1}{4}\left(1 + 2\hat{a}^\dagger\hat{a} - \hat{a}^2 - \hat{a}^{\dagger\,2}\right) \,. \end{aligned} \tag{2.31}$$

Once we have computed the expectations, the state's quadrature space diagram representation will look something like Fig. 2.3.

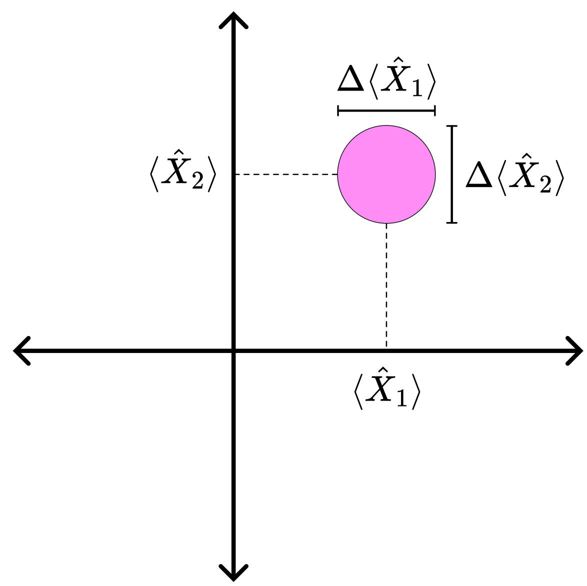

Fig. 2.3: Arbitrary representation of a state in the phase space. The circular shape is for the example (this looks like a coherent state), but depends on the state.

Lastly, for this section, let us recall Heisenberg's minimum uncertainty principle, which, for the quadratures, reads

$$\Delta\left\langle\hat{X}(\nu)\right\rangle\Delta\left\langle\hat{X}\left(\nu+\frac{\pi}{2}\right)\right\rangle \geq \frac{1}{4}\,. \tag{2.32}$$

Effectively, this principle establishes a minimum error area that one state can occupy inthe quadrature space. If a state reaches the equality in Eq. (2.32), we say it is a minimum uncertainty state.

Developing Heisenberg's uncertainty principle with classical and quantum states leads respectively to the standard quantum limit (SQL) and the Heisenberg limit. These limits describe how the minimum uncertainty achievable in a measurement scales with the number of photons (or the energy in the system). The scalings are:

$$\Delta_{\mathrm{SQL}} \sim \frac{1}{\sqrt{N}} \, ,$$
$$\Delta_H \sim \frac{1}{N} \, ,$$

where N is the photon number in the system. The SQL represents the minimum uncertainty achievable using only classical states, whereas the Heisenberg limit applies any kind of state, and it is considered unbreakable. In quantum metrology, the objective is to approach the Heisenberg limit as closely as possible.

2.2.4. Fock States

As a consequence of the quantization of the electromagnetic field, we encounter new quantum states of light, such as the Fock states. These describe the energy quantization. As will be discussed, Fock states do not resemble classical light nor have a classical counterpart, yet they are the simplest quantum light states and are useful for several reasons.

We have already seen that the Hamiltonian of the system is an independent sum over every mode. For simplicity, we now consider a single-mode field, such that every photon has a frequency ω. The Hamiltonian then becomes

$$\hat{H} = \hbar\omega \left(\hat{a}^\dagger \hat{a} + \frac{1}{2}\hat{I} \right) \, . \tag{2.33}$$

Here, the operator $\hat{a}^\dagger \hat{a}$ is called the number operator, also denoted as $\hat{n}$. Fock states are also known as "number states", because they are defined as eigenstates of the number operator, with the eigenvalue representing the precise photon number in the state, as will be shown. For now, let us note that this also means that Fock states are eigenstates of the Hamiltonian. Denoting a Fock state as $|n\rangle$, we have

$$\hat{H}|n\rangle = E_n|n\rangle\,, \tag{2.34}$$

where E_n is the eigenenergy associated with $|n\rangle$. If we evaluate the commutator of the ladder operators with the Hamiltonian using Eqs. (2.16) and (2.18), we obtain

$$\begin{aligned} \left[\hat{H},\hat{a}\right] &= -\hbar\omega\hat{a}\,, \\ \left[\hat{H},\hat{a}^{\dagger}\right] &= \hbar\omega\hat{a}^{\dagger}\,, \end{aligned} \tag{2.35}$$

and using these results, one can show that

$$\begin{aligned} \hat{H}\left(\hat{a}|n\rangle\right) &= \left(E_n - \hbar\omega\right)\left(\hat{a}|n\rangle\right)\,, \\ \hat{H}\left(\hat{a}^{\dagger}|n\rangle\right) &= \left(E_n + \hbar\omega\right)\left(\hat{a}^{\dagger}|n\rangle\right)\,. \end{aligned} \tag{2.36}$$

As clearly shown by Eq. (2.36), the annihilation and creation operators lower and raise the energy of the state $|n\rangle$ by the energy of one photon, $\hbar\omega$, respectively, which is why they are called as such: they remove or add a photon to the system. Since we are basically dealing with a harmonic oscillator, we can not have negative energy values, so there must be a state with minimum energy. Note that this also means that this state lives in the kernel of $\hat{a}$. Let us denote this ground state as $|0\rangle$, then we have

$$\hat{H}|0\rangle = \frac{1}{2}\hbar\omega|0\rangle\,, \tag{2.37}$$

thus, the lowest energy we can have is $E_0 = \frac{1}{2}\hbar\omega$. The other energies are then given by

$$E_n = \hbar\omega\left(n + \frac{1}{2}\right) , \tag{2.38}$$

where $n \in \mathbb{N}_0$. Substituting Eq. (2.38) in (2.34) leads to the fact mentioned earlier:

$$\hat{n}|n\rangle = \hat{a}^\dagger\hat{a}|n\rangle = n|n\rangle , \tag{2.39}$$

where n is the photon number, making their alternative name (number states) clearer.

As for the normalization of Fock states, we note from Eq. (2.36) that

$$\hat{a}|n\rangle = c_n|n-1\rangle , \tag{2.40}$$

with c_n a constant. Using Eqs. (2.39) and (2.40), we can find this constant:

$$\begin{aligned} n &= \langle n|\hat{a}^\dagger\hat{a}|n\rangle \\ &= (\hat{a}|n\rangle)^\dagger\hat{a}|n\rangle \\ &= \langle n-1|c_n^* c_n|n-1\rangle \\ &= |c_n|^2 , \end{aligned}$$

since we want normalized Fock states. We can take $c_n = \sqrt{n}$, and with an analogous procedure for the creation operator, we end up with

$$\begin{aligned} \hat{a}|n\rangle &= \sqrt{n}|n-1\rangle , \\ \hat{a}^\dagger|n\rangle &= \sqrt{n+1}|n+1\rangle . \end{aligned} \tag{2.41}$$

It is now clear that we can generate any Fock state from the ground state using the creation operator as

$$|n\rangle = \frac{\left(\hat{a}^{\dagger}\right)^{n}}{\sqrt{n!}}|0\rangle\,. \tag{2.42}$$

Aside from the normalization, since the Hamiltonian is a Hermitian operator, Fock states are orthogonal for different n values, although one can demonstrate this from Eq. (2.42) and recursively use the commutation rules in Eq. (2.16). We have shown that Fock states are orthonormal, and therefore, form a complete basis of the Hilbert space, expressed by the closure relation:

$$\sum_{n=0}^{\infty} |n\rangle\langle n| = \hat{I}\,. \tag{2.43}$$

To comprehend the behavior of these states, we first take the expectation value of the quadratures in Eq. (2.25), which clearly gives

$$\langle n|\hat{X}_1|n\rangle = \langle n|\hat{X}_2|n\rangle = 0\,. \tag{2.44}$$

This means that Fock states are always centered at the origin of the phase space defined by the quadratures, which does not resemble classical behavior, as this would imply sinusoidal oscillations of some kind. Besides these expectations, we can develop the expectation of the (single mode) electric field operator in Eq. (2.28) by substituting Eqs. (2.25) into it, obtaining

$$\langle n|\hat{E}|n\rangle = 0\,, \tag{2.45}$$

once again, showing that Fock states does not resemble classical light. As for the uncertainty in the quadratures, we take the expectation value of Eq. (2.31),

$$\langle n|\hat{X}_1^2|n\rangle = \langle n|\hat{X}_2^2|n\rangle = \frac{1}{4}(1+2n)\,,$$

and finally

$$\Delta\langle\hat{X}_1\rangle = \Delta\langle\hat{X}_2\rangle = \frac{1}{2}\sqrt{1+2n}\,. \tag{2.46}$$

Here, we can note that the vacuum quadrature fluctuations are $\frac{1}{2}$, making it a minimum uncertainty state, and that Fock states have extra noise associated with them, in addition to the vacuum noise. Fock states are not of minimum uncertainty, since $\Delta\hat{X}_1\Delta\hat{X}_2 > \frac{1}{4}$. With these observations, we can represent a Fock state in the quadrature space, as shown in Fig. 2.4.

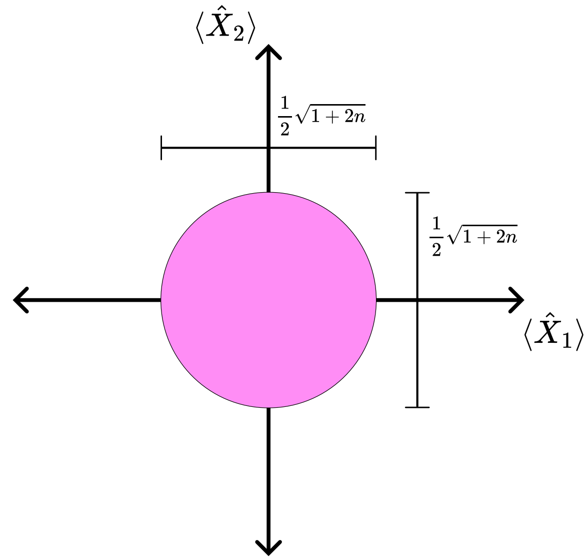

Fig. 2.4: Quadrature space representation for a Fock state.

As seen in Fig. 2.4, Fock states do not have a well-defined phase in this space, as they exhibit angular symmetry. This characteristic will be discussed in Section 2.2.5.

Next, let us assess the fluctuations of the electric field. Using Eq. (2.17), we compute

$$\langle n|\hat{E}^2|n\rangle = \mathcal{E}_0^2\langle n|1 + 2\hat{a}^\dagger\hat{a} - \hat{a}^2e^{2i\varphi} - \hat{a}^{\dagger\,2}e^{-2i\varphi}|n\rangle = \mathcal{E}_0^2(1+2n)\,.$$

From this result, along with Eq. (2.45), we obtain the fluctuations:

$$\Delta\langle\hat{E}\rangle = \mathcal{E}_0\sqrt{1+2n}\,. \tag{2.47}$$

This once again shows that Fock states experience increased noise as the photon number increases. Additionally, the fluctuations for the vacuum state are simply $\mathcal{E}_0$, representing the field amplitude due to a single photon.

Lastly, let us calculate the fluctuations in the photon number. This is given by:

$$\begin{aligned}\Delta\langle\hat{n}\rangle &= \sqrt{\langle n|\hat{a}^\dagger\hat{a}^\dagger\hat{a}\hat{a} + \hat{a}^\dagger\hat{a}|n\rangle - \langle n|\hat{a}^\dagger\hat{a}|n\rangle^2} \\ &= n(n-1) + n - n^2 \\ &= 0\,,\end{aligned} \tag{2.48}$$

implying that Fock states have a well defined photon number.

2.2.5. Quantum Phase

As we know, classical light possesses a well-defined phase during its propagation, and it is natural to desire a similar property for quantum light. Dirac proposed the first method to address this by factorizing the ladder operators as [39]:

$$\begin{aligned}\hat{a} &= e^{i\hat{\phi}}\sqrt{\hat{n}}\,, \\ \hat{a}^\dagger &= \sqrt{\hat{n}}e^{-i\hat{\phi}}\,,\end{aligned} \tag{2.49}$$

where $\hat{\phi}$ was intended to be a Hermitian operator capable of retrieving the phase of the state. However, this approach had a significant flaw: if $\hat{\phi}$ is Hermitian, then $e^{i\hat{\phi}}$ should be unitary. Yet, this was not the case [22]. One proposed solution was to include non-physical Fock states for negative photon numbers, thus removing the lower bound of the $\hat{n}$ spectrum.

Later, Susskind and Glogower proposed [40] an alternative approach, introducing the Susskind-Glogower (SG) operators defined as:

$$\begin{aligned} \hat{e} &= \left(\hat{a}\hat{a}^\dagger\right)^{-\frac{1}{2}} \hat{a}\,, \\ \hat{e}^\dagger &= \hat{a}^\dagger \left(\hat{a}\hat{a}^\dagger\right)^{-\frac{1}{2}}\,. \end{aligned} \tag{2.50}$$

These operators, also referred to as exponential operators, serve as quantum analogs of $\exp(\pm i\phi)$, as we will show. When applied to Fock states, the exponential operators perform transformations analogous to the $e^{\pm i\hat{\phi}}$ operators defined by Dirac:

$$\begin{aligned} \hat{e}|n\rangle &= |n-1\rangle\,, \\ \hat{e}^\dagger|n\rangle &= |n+1\rangle\,. \end{aligned} \tag{2.51}$$

These are similar to the ladder operators, but without the multiplicative constants.

Another useful representation of these operators is:

$$\begin{aligned} \hat{e} &= \sum_{n=0}^{\infty} |n\rangle\langle n+1|\,, \\ \hat{e}^\dagger &= \sum_{n=0}^{\infty} |n+1\rangle\langle n|\,. \end{aligned} \tag{2.52}$$

Using this form, we find that $\hat{e}\hat{e}^\dagger = \hat{I}$, but $\hat{e}^\dagger\hat{e} = \hat{I} - |0\rangle\langle 0|$. Therefore, the SG operators are almost unitary, spoiled by a vacuum contribution. This limitation is relatively acceptable because, for states with sufficiently large photon numbers, the vacuum contribution becomes negligible, and $\hat{e}$ can be considered approximately unitary.

Now that we have a promising candidate to study the quantum phase, let us proceed to further analyze its properties. Since the SG operators are intended to serve as analogs of $e^{\pm i\phi}$, we next consider the eigenvalue problem:

$$\hat{e}|\phi\rangle = e^{i\phi}|\phi\rangle \,, \tag{2.53}$$

where the phase eigenstate is given in the Fock basis by

$$|\phi\rangle = \sum_{n=0}^{\infty} e^{in\phi}|n\rangle \,. \tag{2.54}$$

These eigenstates are neither normalizable nor orthogonal, as their inner product is given by:

$$\langle\phi'|\phi\rangle = \sum_{n=0}^{\infty} e^{in(\phi-\phi')} \neq \delta(\phi-\phi') \,. \tag{2.55}$$

If the spectrum of $\hat{n}$ were unbounded from below, the equality would hold, allowing for the orthonormalization of the phase eigenstates. Nevertheless, we achieve a form of normalization by noting that

$$\frac{1}{2\pi}\int_0^{2\pi} |\phi\rangle\langle\phi|d\phi = 1 \,. \tag{2.56}$$

This normalization introduces the perspective of associating a phase distribution with quantum states. For a normalized state $|\psi\rangle$, expressed as:

$$|\psi\rangle = \sum_{n=0}^{\infty} C_n|n\rangle \,, \tag{2.57}$$

we can define the phase distribution associated with $|\psi\rangle$ using Eq. (2.54) as:

$$\begin{aligned}\mathcal{P}(\phi) &\equiv \frac{1}{2\pi}|\langle\phi|\psi\rangle|^2 \\ &= \frac{1}{2\pi}\left|\sum_{n=0}^{\infty} e^{-in\phi}C_n\right|^2 \,,\end{aligned} \tag{2.58}$$

which is always positive and normalized when integrated, as shown in Eq. (2.56).

This allows us to compute the average of any function $f(\phi)$ according to:

$$\langle f(\phi)\rangle = \int_0^{2\pi} f(\phi)\mathcal{P}(\phi)d\phi\,. \tag{2.59}$$

The average $\langle\phi\rangle$ is the closest analog to a quantum phase. For example, consider a Fock state $|n\rangle$. From Eq. (2.58), its phase distribution is $\mathcal{P}(\phi) = \frac{1}{2\pi}$, indicating that all values of ϕ are equally probable. Combined with the fact that $\Delta\langle\hat{n}\rangle = 0$, this confirms that Fock states appear as circles in the phase space (see Fig. 2.4).

2.2.6. Coherent States

As discussed in section 2.2.4, Fock states are not well-suited as quantum analogs to describe classical light. This is because they lack a fixed phase, and the expectation value of the electric field operator is zero, rather than sinusoidal. However, there exists a quantum state of light that closely resembles the behavior of classical light in many aspects: the **coherent states**. These states are considered the most classical among quantum states, although they still exhibit inherently quantum behavior [41, 42].

Mathematically, coherent states are defined as eigenstates of the annihilation operator:

$$\hat{a}|\alpha\rangle = \alpha|\alpha\rangle\,, \tag{2.60}$$

where $|\alpha\rangle$ is the coherent state corresponding to the complex eigenvalue α. The complex parameter α naturally encodes both the amplitude and phase of the coherent state, which correspond directly to the amplitude and phase of α itself. This can be demonstrated by evaluating the expectation value of the quadratures in Eq. (2.25) for a coherent state as:

$$\begin{aligned} \langle\alpha|\hat{X}_1|\alpha\rangle &= \frac{1}{2}\langle\alpha|\hat{a}^\dagger + \hat{a}|\alpha\rangle\,, \\ \langle\alpha|\hat{X}_2|\alpha\rangle &= \frac{1}{2i}\langle\alpha|\hat{a} - \hat{a}^\dagger|\alpha\rangle\,. \end{aligned} \tag{2.61}$$

To calculate these expectation values, we use the Hermitian conjugate of Eq. (2.60):

$$\langle\alpha|\hat{a}^\dagger = \alpha^*\langle\alpha|\,. \tag{2.62}$$

Substituting Eqs. (2.60) and (2.62) into Eq. (2.61), we obtain:

$$\begin{aligned} \langle\alpha|\hat{X}_1|\alpha\rangle &= \frac{\alpha^* + \alpha}{2} = \Re(\alpha)\,, \\ \langle\alpha|\hat{X}_2|\alpha\rangle &= \frac{\alpha - \alpha^*}{2i} = \Im(\alpha)\,. \end{aligned} \tag{2.63}$$

Here, we assume that coherent states are normalized. The results in Eqs. (2.63) demonstrate that, in the phase space defined by these quadratures, the coherent state's amplitude and phase correspond directly to those of α. Writing $\alpha = |\alpha|e^{i\theta}$, we can compute the expectation value of the electric field operator from Eq. (2.17), resulting in (for a single mode field):

$$\begin{aligned} \langle\alpha|\hat{E}|\alpha\rangle &= i\mathcal{E}_0\left(\langle\alpha|\hat{a}|\alpha\rangle e^{i\varphi} - \langle\alpha|\hat{a}^\dagger|\alpha\rangle e^{-i\varphi}\right) \\ &= i\mathcal{E}_0\left(\alpha e^{i\varphi} - \alpha^* e^{-i\varphi}\right) \\ &= -2|\alpha|\mathcal{E}_0 \sin\left(\varphi + \theta\right)\,, \end{aligned} \tag{2.64}$$

which resembles a classical field. Therefore, we have a quantum state with a well-defined amplitude and phase (in the phase space defined by the quadratures), and the expectation value of the electric field for these states behaves like in classical mechanics. This makes coherent states a "quasi-classical" estate of light. What are the quantum features of coherent states then? Naturally, **uncertainty**.

Let us calculate the fluctuations in the quadrature space. By taking the expectation value of Eq. (2.31) in a coherent state and using Eqs. (2.60) and (2.62), we find

$$\begin{aligned}\langle\alpha|\hat{X}_1^2|\alpha\rangle &= \frac{1}{4} + |\alpha|^2\cos^2\theta\,,\\ \langle\alpha|\hat{X}_2^2|\alpha\rangle &= \frac{1}{4} + |\alpha|^2\sin^2\theta\,.\end{aligned}$$

Using Eqs. (2.63), it becomes clear that

$$\Delta\langle\hat{X}_1\rangle = \Delta\langle\hat{X}_2\rangle = \frac{1}{2}\,. \tag{2.65}$$

This means that the noise in both quadratures is $\frac{1}{2}$ for any coherent state, which is the same as the vacuum state. Coherent states are minimum uncertainty states, as they saturate the uncertainty principle, and they exhibit equal uncertainties in both quadratures. These properties provide an alternative way to define coherent states, as they describe how these states are represented in phase space: a circle centered in α with diameter $\frac{1}{2}$, as illustrated in Fig. 2.5.

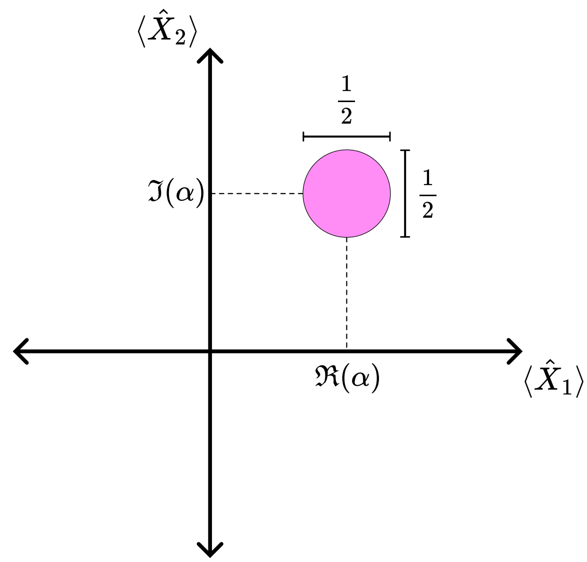

Fig. 2.5: Quadrature space representation of the coherent state $|\alpha\rangle$.

For the uncertainty in the field operator, we need the expectation value of $\hat{E}^2$. Starting from Eq. (2.17), we proceed as follows:

$$
\begin{aligned}
\langle\alpha|\hat{E}^2|\alpha\rangle &= \mathcal{E}_0^2 \left\langle \alpha \left| 1 + 2\hat{a}^\dagger \hat{a} - \hat{a}^2 e^{2i\varphi} - \hat{a}^{\dagger\, 2} e^{-2i\varphi} \right| \alpha \right\rangle \\
&= \mathcal{E}_0^2 \left(1 + 2|\alpha|^2 - \alpha^2 e^{2i\varphi} - \alpha^{*2} e^{-2i\varphi} \right) \\
&= \mathcal{E}_0^2 \Big(1 + 2|\alpha|^2 \Big(1 - \cos\left(2(\varphi+\theta)\right) \Big) \Big) \\
&= \mathcal{E}_0^2 \left(1 + 4|\alpha|^2 \sin^2(\varphi+\theta) \right) \,. \qquad (2.66)
\end{aligned}
$$

Now, with Eqs. (2.64) and (2.66), it is clear that the fluctuations of the electric field are

$$
\Delta\langle\hat{E}\rangle = \mathcal{E}_0 \,, \qquad (2.67)
$$

which are the vacuum fluctuations as well. Although these fluctuations are due to the quantum nature of coherent states, the fact that they are those of the vacuum makes these states nearly classical. This is because the vacuum noise is always present; they have no additional noise associated with the coherent state itself, unlike Fock states.

At this point, we have showed that coherent states are a viable way to represent classical light in quantum mechanics.

Now, we study the photon distribution in coherent states. For this, we first obtain the expected photon number with the number operator. We get

$$\langle \hat{n} \rangle = \langle \alpha | \hat{n} | \alpha \rangle = |\alpha|^2 \,. \tag{2.68}$$

Not a surprise, since $|\alpha|$ is the amplitude of the field, the intensity must be $|\alpha|^2$. For the fluctuations in the mean photon number, it is easy to show that

$$\Delta \langle \hat{n} \rangle = \sqrt{\langle \alpha | \hat{a}^\dagger \hat{a}^\dagger \hat{a} \hat{a} + \hat{a}^\dagger \hat{a} | \alpha \rangle - \langle \alpha | \hat{a}^\dagger \hat{a} | \alpha \rangle^2} = |\alpha| = \sqrt{\langle \hat{n} \rangle} \,. \tag{2.69}$$

This result is what we expect for a Poissonian distribution. We notice that the relative uncertainty in the mean photon number holds

$$\frac{\Delta \langle \hat{n} \rangle}{\langle \hat{n} \rangle} = \frac{1}{\sqrt{\langle \hat{n} \rangle}} \,, \tag{2.70}$$

which becomes smaller as the mean photon number increases. This means that with a large enough number of photons, coherent states behave like a classical state.

To see the origin of the Poissonian behaviour of coherent states, let us recall that Fock states form a basis for the Hilbert space, so we can write a coherent (or any) state as

$$|\alpha\rangle = \sum_{n=0}^{\infty} C_n |n\rangle \,, \tag{2.71}$$

with C_n complex. Acting with $\hat{a}$,

$$\begin{aligned} \hat{a}|\alpha\rangle &= \sum_{n=0}^{\infty} C_n \hat{a}|n\rangle \\ &= \sum_{n=1}^{\infty} C_n \sqrt{n}|n-1\rangle \,, \qquad (2.72) \\ \alpha|\alpha\rangle &= \sum_{n=0} \alpha C_n |n\rangle \,. \qquad (2.73) \end{aligned}$$

Equating the terms of $|n\rangle$ in Eqs. (2.72) and (2.73) we arrive at

$$C_n = \frac{\alpha}{\sqrt{n}} C_{n-1} \,,$$

which means

$$C_n = \frac{\alpha^n}{\sqrt{n!}} C_0 \,,$$

so

$$|\alpha\rangle = C_0 \sum_{n=0}^{\infty} \frac{\alpha^n}{\sqrt{n!}} |n\rangle \,. \tag{2.74}$$

For C_0, we evaluate the normalization condition,

$$\begin{aligned} \langle\alpha|\alpha\rangle &= |C_0|^2 \sum_{n'=0}^{\infty} \sum_{n=0}^{\infty} \frac{\alpha^{*n'} \alpha^n}{\sqrt{n'! n!}} \langle n'|n\rangle \\ &= |C_0|^2 \sum_{n=0}^{\infty} \frac{|\alpha|^{2n}}{n!} \end{aligned}$$

$$= |C_0|^2 e^{|\alpha|^2} \, .$$

Thus, $C_0 = \exp\left(-\frac{1}{2}|\alpha|^2\right)$ satisfies the normalization condition, resulting in coherent states being represented as

$$|\alpha\rangle = \exp\left(-\frac{1}{2}|\alpha|^2\right) \sum_{n=0}^{\infty} \frac{\alpha^n}{\sqrt{n!}} |n\rangle \, . \tag{2.75}$$

Now, using Eq. (2.69), the probability of detecting n photons is

$$P_n = |C_n|^2 = \exp\left(-|\alpha|^2\right) \frac{|\alpha|^{2n}}{n!} = e^{-\langle\hat{n}\rangle} \frac{\langle\hat{n}\rangle^n}{n!} \, , \tag{2.76}$$

which is exactly a Poisson distribution with mean $\langle\hat{n}\rangle$. Now, for the phase distribution of coherent sates, we use Eqs. (2.58) and (2.75) to get

$$\mathcal{P}(\phi) = \frac{1}{2\pi} e^{-|\alpha|^2} \left| \sum_{n=0}^{\infty} e^{in(\theta-\phi)} \frac{|\alpha|^n}{\sqrt{n!}} \right|^2 \, ,$$

where $\alpha = |\alpha| e^{i\theta}$. For large enough $|\alpha|^2$, a Poissonian distribution approximates to a Gaussian, so in this case we may write

$$\mathcal{P}(\phi) \approx \sqrt{\frac{2|\alpha|^2}{\pi}} \exp\left(-2|\alpha|^2 \left(\phi - \theta\right)^2\right) \, . \tag{2.77}$$

This is a Gaussian centered at $\phi = \theta$. It is also worth noting that for increasing photon number the Gaussian becomes narrower, resembling better classical light due to its now well-defined phase.

Finally, for coherent states, let us think again about their phase space representation (see Fig. 2.5). When changing the complex parameter α, we are effectively *displacing* the circle over the phase space. This gives us the hint of considering coherent states as displaced vacuum states, and so we define the displacement operator $\hat{D}(\alpha)$ according to

$$\hat{D}(\alpha)|0\rangle = |\alpha\rangle \,. \tag{2.78}$$

To express this operator, we substitute Eq. (2.42) in Eq. (2.75) to get

$$\begin{aligned} |\alpha\rangle &= \exp\left(-\frac{1}{2}|\alpha|^2\right) \sum_{n=0}^{\infty} \frac{\alpha^n}{n!} \hat{a}^{\dagger\, n} |0\rangle \\ &= \exp\left(-\frac{1}{2}|\alpha|^2\right) \exp\left(\alpha \hat{a}^\dagger\right) |0\rangle \,. \end{aligned} \tag{2.79}$$

Here one could claim that the displacement operator is $\exp\left(-\frac{1}{2}|\alpha|^2\right) \exp\left(\alpha\hat{a}^\dagger\right)$, but it is not yet complete, because it is a non-unitary transformation, as one can easily test. To solve this, we notice that

$$\exp\left(-\alpha^* \hat{a}\right) |0\rangle = \sum_{n=0}^{\infty} \frac{\left(-\alpha^* \hat{a}\right)^n}{\sqrt{n!}} |0\rangle = |0\rangle \,,$$

so Eq. (2.79) becomes

$$|\alpha\rangle = \exp\left(-\frac{1}{2}|\alpha|^2\right) \exp\left(\alpha\hat{a}^\dagger\right) \exp\left(-\alpha^* \hat{a}\right) |0\rangle \,. \tag{2.80}$$

To Further develop this, we note that

$$\left[\alpha\hat{a}^\dagger, -\alpha^* \hat{a}\right] = |\alpha|^2 \,,$$

so this commutator commutes with anything. Then, by the Baker-Campbell-Hausdorff formula (BCH),

$$\exp\left(\alpha\hat{a}^\dagger\right) \exp\left(-\alpha^* \hat{a}\right) = \exp\left(\alpha\hat{a}^\dagger - \alpha^* \hat{a} + \frac{1}{2}|\alpha|^2\right) \,,$$

and substituting this in Eq. (2.80), we get the final expression for the displacement operator:

$$\hat{D}(\alpha) = \exp\left(-\frac{1}{2}|\alpha|^2\right)\exp\left(\alpha\hat{a}^\dagger\right)\exp\left(-\alpha^*\hat{a}\right) = \exp\left(\alpha\hat{a}^\dagger - \alpha^*\hat{a}\right) \,. \tag{2.81}$$

The displacement operator in Eq. (2.81) is now unitary. Practically speaking, what this operator does is create photons in the system one by one, as we can see from Eq. (2.79). Utilizing the BCH formula one can easily show the relevant properties of this operator:

1. **Unitary operator:** This means that $\hat{D}(\alpha)\hat{D}^\dagger(\alpha) = \hat{D}^\dagger(\alpha)\hat{D}(\alpha) = \hat{I}$. In fact, we can note that $\hat{D}^\dagger(\alpha) = \hat{D}(-\alpha)$, so inverting the action of the operator is equivalent to displacing in the opposite direction. This property is achieved by making the operator unitary.

2. **Displaced ladder operators:** When we let the ladders operators evolve with the displacement operator, we get

$$\begin{aligned} \hat{D}^\dagger(\alpha)\hat{a}\hat{D}(\alpha) &= \hat{a} + \alpha\hat{I} \,, \\ \hat{D}^\dagger(\alpha)\hat{a}^\dagger\hat{D}(\alpha) &= \hat{a}^\dagger + \alpha^*\hat{I} \,. \end{aligned} \tag{2.82}$$

3. **Non-cumulative displacement:** It would be nice if $\hat{D}(\alpha)\hat{D}(\beta) = \hat{D}(\alpha + \beta)$, but the truth is that these results differ by a phase factor, leading to $\hat{D}(\alpha)\hat{D}(\beta) = \exp\left(i\Im(\alpha\beta^*)\right)\hat{D}(\alpha+\beta)$. This phase shift is physically irrelevant, as it does not change the photon distribution. Still, we can note that if α and β are either parallel or anti-parallel, there is no phase shift. This property also leads to non-commutativity, indeed, $\hat{D}(\alpha)\hat{D}(\beta) = \exp\left(2i\Im(\alpha\beta^*)\right)\hat{D}(\beta)\hat{D}(\alpha)$.

2.2.7. Squeezed States

Up to this section, we have only encountered states with symmetric quadrature uncertainty. Squeezed states, while being minimum uncertainty states, exhibit different uncertainties in each quadrature. This is achieved by increasing the uncertainty in one quadrature while decreasing it in the other, which is useful due to the enhanced precision when measuring the squeezed quadrature.

To generate these states, we consider a non-linear operator analogous to the displacement operator:

$$\hat{S}(\xi) = \exp\left(\frac{1}{2}\left(\xi^* \hat{a}^2 - \xi \hat{a}^{\dagger\,2}\right)\right) . \tag{2.83}$$

This is the squeezing operator, and unlike the displacement operator, the creation of photons in squeezed states occurs in pairs. A squeezed state[3] is denoted as

$$|\xi\rangle = \hat{S}(\xi)|0\rangle . \tag{2.84}$$

We can also interpret this by noting that the displacement operator arises from the evolution due to a Hamiltonian of the form

$$\hat{H} \propto \alpha \hat{a}^\dagger - \alpha^* \hat{a} .$$

With this Hamiltonian the propagator is

$$\exp\left(\frac{i}{\hbar}\hat{H}t\right) = \hat{D}\left(\alpha t\right) .$$

[3] More precisely, this is a squeezed vacuum state.

Therefore, we interpret squeezed states as those that arises from the evolution due to a Hamiltonian of the form

$$\hat{H} \propto \xi^* \hat{a}^2 - \xi \hat{a}^{\dagger\,2}\,.$$

For the squeezing operator, the main properties can also be derived using the BCH formula. These properties are:

1. **Unitary operator:** $\hat{S}^\dagger(\xi) = \hat{S}^{-1}(\xi)$. For the squeezing operator, we also note that $\hat{S}^\dagger(\xi) = \hat{S}(-\xi)$. As we progress in this section, we will interpret what squeezing in the opposite direction means.

2. **Squeezed ladder operators:** Evolving the ladder operators with the squeezing operator leads to

$$\begin{aligned} \hat{S}^\dagger(\xi)\hat{a}\hat{S}(\xi) &= \hat{a}\cosh(r) - \hat{a}^\dagger e^{i\theta}\sinh(r) = \hat{a}_s\,, \\ \hat{S}^\dagger(\xi)\hat{a}^\dagger \hat{S}(\xi) &= \hat{a}^\dagger \cosh(r) - \hat{a}e^{-i\theta}\sinh(r) = \hat{a}_s^\dagger\,, \end{aligned} \tag{2.85}$$

where we have taken $\xi = re^{i\theta}$. Note that these are linear combinations of the ladder operators.

For computing the quadrature expectation values for squeezed states, we use Eq. (2.85). We arrive at

$$\begin{aligned} \langle\xi|\hat{X}(\nu)|\xi\rangle &= \frac{1}{2}\langle 0|\hat{S}^\dagger(\xi)\left(\hat{a}e^{-i\nu} + \hat{a}^\dagger e^{i\nu}\right)\hat{S}(\xi)|0\rangle \\ &= \frac{1}{2}\left\langle 0\left|\hat{a}_s e^{-i\nu} + \hat{a}_s^\dagger e^{i\nu}\right| 0\right\rangle \\ &= 0\,. \end{aligned} \tag{2.86}$$

For any quadrature we may choose, the expectation is 0, so the state is centered at the origin of the quadrature space.

Therefore, the expectation of the electric field is

$$\langle\xi|\hat{E}|\xi\rangle = 0\,. \tag{2.87}$$

The uncertainties are not as straightforward as before due to the nonlinear effects. We must compute the expectation values of quadratic combinations of the ladder operators. To achieve this, we recall Eq. (2.85) and we develop the following:

$$\hat{S}^\dagger(\xi)\hat{A}\hat{B}\hat{S}(\xi) = \hat{S}^\dagger(\xi)\hat{A}\hat{S}(\xi)\hat{S}^\dagger(\xi)\hat{B}\hat{S}(\xi) = \hat{A}_s\hat{B}_s\,, \tag{2.88}$$

where $\hat{A}$ and $\hat{B}$ are arbitrary operators, and their squeezed representations are denoted with an s subscript. Thus, utilizing Eq. (2.85), we arrive at

$$\begin{aligned}
\hat{S}^\dagger(\xi)\hat{a}^2\hat{S}(\xi) &= \hat{a}_s^2 = \hat{a}^2\cosh^2 r + \hat{a}^{\dagger\,2}e^{2i\theta}\sinh^2 r - \left(1+2\hat{a}^\dagger\hat{a}\right)e^{i\theta}\cosh r\sinh r\,,\\
\hat{S}^\dagger(\xi)\hat{a}^{\dagger\,2}\hat{S}(\xi) &= \hat{a}_s^{\dagger\,2} = \hat{a}^2 e^{-2i\theta}\sinh^2 r + \hat{a}^{\dagger\,2}\cosh^2 r - \left(1+2\hat{a}^\dagger\hat{a}\right)e^{-i\theta}\cosh r\sinh r\,,\\
\hat{S}^\dagger(\xi)\hat{a}^\dagger\hat{a}\hat{S}(\xi) &= \hat{a}_s^\dagger\hat{a}_s = \sinh^2 r + \hat{a}^\dagger\hat{a}\cosh(2r) - \left(\hat{a}^2 e^{-i\theta} + \hat{a}^{\dagger\,2}e^{i\theta}\right)\cosh r\sinh r\,.
\end{aligned} \tag{2.89}$$

With this, we derive the quadrature uncertainties by substituting Eq. (2.89) into Eq. (2.30), which gives

$$\begin{aligned}
\langle\xi|\hat{X}^2(\nu)|\xi\rangle &= \frac{1}{4}\left\langle 0\left|1+2\hat{a}_s^\dagger\hat{a}_s + \hat{a}_s^2 e^{-2i\nu} + \hat{a}_s^{\dagger\,2}e^{2i\nu}\right|0\right\rangle\\
&= \frac{1}{4}\Bigg(\cosh(2r) - \cos(\theta-2\nu)\sinh(2r)\Bigg)\,.
\end{aligned}$$

The fluctuation are therefore

$$\Delta\left\langle \hat{X}(\nu)\right\rangle = \frac{1}{2}\sqrt{\cosh(2r) - \cos(\theta - 2\nu)\sinh(2r)}\,. \tag{2.90}$$

These fluctuations have a maximum and minimum value depending on the phases of the quadratures and complex squeezing parameter. The extremes are as follows:

$$\Delta\left\langle \hat{X}(\nu)\right\rangle = \begin{cases} \dfrac{1}{2}e^{-r}\,, & \text{for } \nu = \dfrac{\theta}{2} \text{ or } \nu = \dfrac{\theta}{2} + \pi, \\ \\ \dfrac{1}{2}e^{r}\,, & \text{for } \nu = \dfrac{\theta}{2} \pm \dfrac{\pi}{2}. \end{cases} \tag{2.91}$$

In this case, we need to adjust the quadrature phases for the squeezed state to be of minimum uncertainty. Once this is done, we gain increased precision when measuring one of the quadratures. In general, the uncertainty product for a pair of quadratures is given by

$$\Delta\left\langle \hat{X}(\nu)\right\rangle \Delta\left\langle \hat{X}\left(\nu + \frac{\pi}{2}\right)\right\rangle = \frac{1}{4}\sqrt{\cosh^2(2r) - \cos^2(\theta - 2\nu)\sinh^2(2r)}\,. \tag{2.92}$$

Thus, squeezed states are minimum uncertainty states only for quadratures holding Eq. (2.91). Given this, a vacuum squeezed state is represented in the quadrature space as in Fig. 2.6.

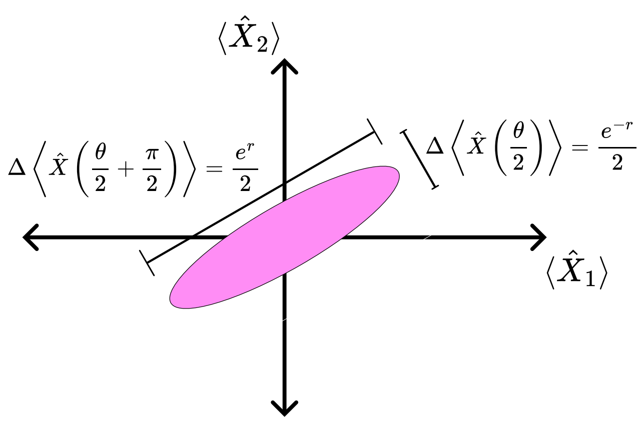

Fig. 2.6: Quadrature space representation of a vacuum squeezed state given by the complex squeezing parameter $\xi = re^{i\theta}$.

For the electric field fluctuations, we first compute from Eq. (2.17):

$$\begin{aligned}\langle\xi|\hat{E}^2|\xi\rangle &= \mathcal{E}_0^2 \left\langle\xi\left|1+2\hat{a}^\dagger\hat{a}-\hat{a}^2e^{2i\varphi}-\hat{a}^{\dagger\,2}e^{-2i\varphi}\right|\xi\right\rangle \\ &= \mathcal{E}_0^2 \left\langle 0\left|1+2\hat{a}_s^\dagger\hat{a}_s-\hat{a}_s^2e^{2i\varphi}-\hat{a}_s^{\dagger\,2}e^{-2i\varphi}\right|0\right\rangle \\ &= \mathcal{E}_0^2 \Big(\cosh(2r)+\cos(\theta+2\varphi)\sinh(2r)\Big)\,. \end{aligned} \tag{2.93}$$

Thus, the field fluctuations are

$$\Delta\langle\hat{E}\rangle = \mathcal{E}_0\sqrt{\cosh(2r)+\cos(\theta+2\varphi)\sinh(2r)}\,. \tag{2.94}$$

For the electric field, the extremes are $\mathcal{E}_0 e^{\pm r}$, depending on the phases. This means that during propagation, the field uncertainty changes, such that at certain instances, one can measure the field with increased precision.

Lastly, let us assess the photon statistics of squeezed states. From Eq. (2.89), we can clearly see that the photon number is now

$$\langle\xi|\hat{n}|\xi\rangle = \sinh^2 r \neq 0\,. \tag{2.95}$$

Squeezed vacuum states are not truly empty from this perspective; nevertheless, they are still considered vacuum states because the field amplitude is zero, as it would be for the ordinary vacuum.

2.2.8. Displaced Squeezed States

We can combine the ideas of coherent and squeezed states to create displaced squeezed states, which are essentially the same as squeezed coherent states or bright squeezed light. They are states with a non-zero field amplitude and squeezed quadrature uncertainties, and are generated by composing the displacement and squeezing operators. They are denoted as

$$|\alpha, \xi\rangle = \hat{D}(\alpha)\hat{S}(\xi)|0\rangle\,, \tag{2.96}$$

where we first squeeze the vacuum and then displace it. Since these two operators do not commute, displacing the vacuum and then squeezing it will not give the same state using the same parameters. However, conceptually, the resulting states will be similar: non-zero field amplitude and squeezed uncertainties. For these two approaches to coincide, a parameter $\gamma = \alpha \cosh r + \alpha^* e^{i\theta} \sinh r$ must hold, such that

$$\hat{D}(\alpha)\hat{S}(\xi) = \hat{S}(\xi)\hat{D}(\gamma)\,,$$

where $\xi = re^{i\theta}$. Without going into the detailed expectation values, a general displaced squeezed states can be represented in the quadrature space as in Fig. 2.7.

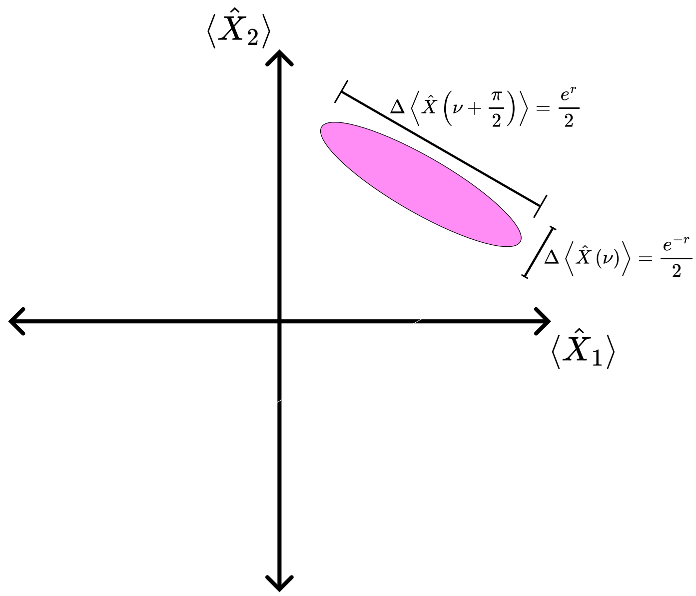

Fig. 2.7: Representation in the quadrature space of an arbitrary displaced squeezed state with squeezing parameter r and assuming an optimal ν.

From Fig. 2.7 it is clear that displaced squeezed states are simply displacements of a vacuum squeezed state. Moreover, the uncertainties are similar to those of the squeezed vacuum state (Fig. 2.6), which is due to the coherent state not having additional uncertainty.

2.2.9. Two-Mode Squeezed States

Another kind of squeezed state are the **two-mode squeezed states**. They arise naturally when single-mode squeezed vacuum states propagate through, e.g., a coupled waveguide array [25, 43].

Mathematically, the non linearity of squeezed states allows for the appearance of the crossed terms $\hat{a}_i\hat{a}_j$ and $\hat{a}_i^\dagger\hat{a}_j^\dagger$ in the squeezed operator's argument after propagating and therefore mixing the annihilation operators. The pure two-mode squeezing operator acting on the i-th and j-th modes is given by

$$\hat{S}_{ij}(\xi) = \exp\left(\frac{1}{2}\left(\xi\hat{a}_i^\dagger\hat{a}_j^\dagger - \xi^*\hat{a}_i\hat{a}_j\right)\right) . \tag{2.97}$$

These states exhibit squeezed uncertainty in a linear combination of the quadratures of the two modes.

As these states arise alongside single-mode squeezed states, we aim to better understand the dynamics governing single- and two-mode squeezing. An initial exploration of this topic can be found in Chapter 4.

Chapter 3

Optical Devices and Techniques

3.1. Standard Two-Port Interferometry

In this section, we explore the interferometry of quantum light, focusing on the standard case of two-port interferometry. In Section 3.1.1, we review the physical and mathematical descriptions relevant to this thesis for 2-input, 2-output beam splitters. Then, in Section 3.1.2, we construct a 2-input, 2-output Mach-Zehnder interferometer using the previously defined beam splitters, demonstrating its use as an optical sensor and showing how the precision of measurements can be improved beyond the standard quantum limit (SQL) using quantum resources.

3.1.1. Two-Port Beam Splitter

A beam splitter (BS) is an optical device that *splits* a light beam into two or more beams. A simple way to achieve this is by simultaneously transmitting and reflecting light. Consider the situation depicted in Fig. 3.1.

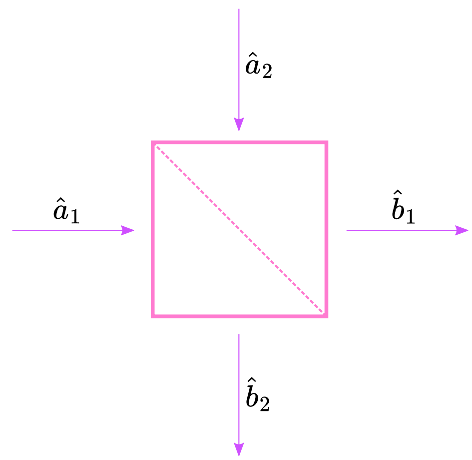

Fig. 3.1: 2 input, 2 output BS (BS_2). $\hat{a}_i$ ($\hat{b}_i$) are the annihilation operators for the i-th path at the input (output).

In Fig. 3.1, we write the annihilation operator where we would typically write the intensity in a classical context, in consideration of the fact that they are analogs to a complex amplitude. To provide an accurate description, we must also account for a second input, considering that the vacuum is always present and to preserve the commutation relations for the ladder operators.[1]

The beam splitter is defined by the transformation

$$\begin{pmatrix} \hat{b}_1 \\ \hat{b}_2 \end{pmatrix} = \begin{pmatrix} t' & r \\ r' & t \end{pmatrix} \begin{pmatrix} \hat{a}_1 \\ \hat{a}_2 \end{pmatrix} , \tag{3.1}$$

where r and t stand for reflection and transmission coefficients, respectively. The conditions for energy conservation are

$$\begin{gathered} |r'| = |r| \, , \, |t'| = |t| \, , \, |r|^2 + |t|^2 = 1 \, , \\ r^* t' + r' t^* = 0 \, , \end{gathered} \tag{3.2}$$

[1]For more classical-like states, such as thermal or sufficiently large coherent states, the vacuum contribution becomes negligible, and a classical description suffices.

$$r^*t + r't'^* = 0\,.$$

These conditions also force the transformation to be unitary.

In the case of a balanced BS, the intensity must be equally distributed across all paths, so $|r| = |r'| = |t| = |t'| = \frac{1}{\sqrt{2}}$. Additionally, if the reflected waves have a phase shift of $\frac{\pi}{2}$ relative to the transmitted wave (which is the usual in commercially available devices), the transformation for the BS is given by

$$\begin{pmatrix} \hat{b}_1 \\ \hat{b}_2 \end{pmatrix} = \frac{1}{\sqrt{2}} \begin{pmatrix} 1 & i \\ i & 1 \end{pmatrix} \begin{pmatrix} \hat{a}_1 \\ \hat{a}_2 \end{pmatrix} . \tag{3.3}$$

The choice of phase shift is entirely arbitrary and depends on the specific construction of the BS. We can account for this arbitrariness by independently shifting the phase in each path before and after the BS, as shown by the following transformation:

$$\begin{pmatrix} \hat{b}_1 \\ \hat{b}_2 \end{pmatrix} = \frac{1}{\sqrt{2}} \begin{pmatrix} e^{i\phi_{o1}} & 0 \\ 0 & e^{i\phi_{o2}} \end{pmatrix} \begin{pmatrix} 1 & i \\ i & 1 \end{pmatrix} \begin{pmatrix} e^{i\phi_{i1}} & 0 \\ 0 & e^{i\phi_{i2}} \end{pmatrix} \begin{pmatrix} \hat{a}_1 \\ \hat{a}_2 \end{pmatrix} . \tag{3.4}$$

The real-bordered transformation for a 2-port BS is then

$$B_2 = \frac{1}{\sqrt{2}} \begin{pmatrix} 1 & 1 \\ 1 & -1 \end{pmatrix} . \tag{3.5}$$

This is the discrete or quantum Fourier transformation, and also a Hadamard transformation. Since the BS transformation is unitary, there exists a unitary operator $\hat{U}_2$ such that

$$\begin{pmatrix} \hat{b}_1 \\ \hat{b}_2 \end{pmatrix} = \hat{U}_2^\dagger \begin{pmatrix} \hat{a}_1 \\ \hat{a}_2 \end{pmatrix} \hat{U}_2\,. \tag{3.6}$$

For the specific transformation in Eq. (3.3), the unitary operator is

$$\hat{U}_2 = \exp\left(i\frac{\pi}{4}\left(\hat{a}_1^\dagger\,\hat{a}_2 + \hat{a}_1\hat{a}_2^\dagger\right)\right) . \tag{3.7}$$

To verify this, one can use the BCH formula. This allows us to describe the BS from another perspective: propagation through a coupled waveguide array. In an optical dimer [25], the evolution operator is

$$\hat{U}_2(\gamma) = \exp\left(\gamma \hat{a}_1^\dagger \hat{a}_2 - \gamma^* \hat{a}_1 \hat{a}_2^\dagger\right) , \tag{3.8}$$

where $\gamma = \theta e^{i\delta}$ is the complex coupling between the waveguides. The balanced beam splitter described in Eq. (3.7) is recovered when $\theta = \frac{\pi}{4}$ and $\delta = \frac{\pi}{2}$. Here, $\theta = \kappa z$, where κ is the coupling constant (spatial frequency) and z the propagation distance. Thus, θ is the relevant dimensionless parameter that evolves the system. The matrix representation of the evolution in Eq. (3.8) is

$$U_{2M}(\theta, \delta) = \begin{pmatrix} \cos\theta & e^{i\delta}\sin\theta \\ -e^{-i\delta}\sin\theta & \cos\theta \end{pmatrix} . \tag{3.9}$$

Both descriptions of the BS are useful in different contexts. The first is used for free-space propagation, and the second applies to waveguide or optical fiber propagation.

3.1.2. Two-Port Mach-Zehnder Interferometer

Now that we have defined the BS, we can proceed to construct an interferometer. Using the free-space approach, the Mach-Zehnder interferometer (MZI) is represented in Figure 3.2.

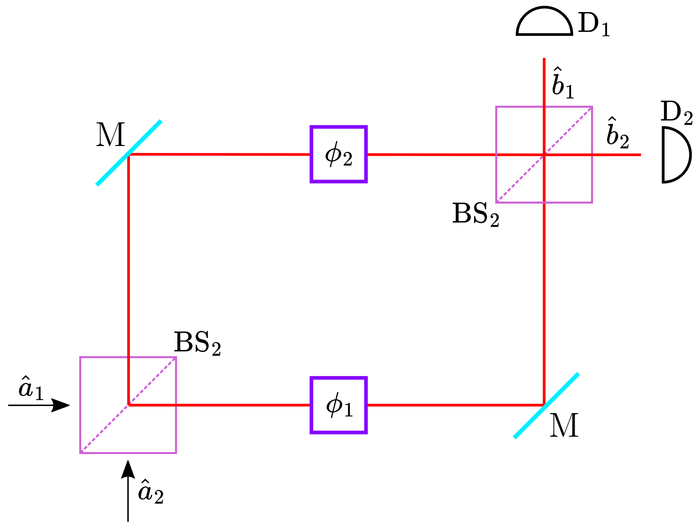

Fig. 3.2: Representation of a 2 input, 2 output Mach-Zehnder interferometer (MZI$_2$). The $\hat{a}_i$ ($\hat{b}_i$) are the annihilation operators at the input (output) of the i-th path, ϕ_i is the phase shift in the i-th path, M are mirrors and D_i are detectors.

As shown in Section 3.1.1, the input and output phases in the BS are arbitrary. Thus, the contribution from the mirrors becomes irrelevant. Therefore, we use a simpler representation of the interferometer, as shown in Figure 3.3, which is valid in both free-space and non-free-space scenarios.

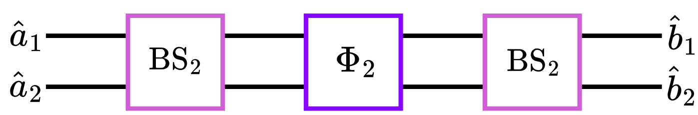

Fig. 3.3: Simple representation of a 2 input, 2 output Mach-Zehnder interferometer. Φ_2 shifts the phase independetely in each path.

The phase shift operator is given by

$$\Phi_2 = \begin{pmatrix} e^{i\phi_1} & 0 \\ 0 & e^{i\phi_2} \end{pmatrix} . \tag{3.10}$$

Thus, considering the BS in Eq. (3.3), the complete transformation of the MZI is

$$M_2 = B_2 \Phi_2 B_2 = \frac{1}{2} \begin{pmatrix} e^{i\phi_1} - e^{i\phi_2} & i\left(e^{i\phi_1} + e^{i\phi_2}\right) \\ i\left(e^{i\phi_1} + e^{i\phi_2}\right) & e^{i\phi_2} - e^{i\phi_1} \end{pmatrix} . \tag{3.11}$$

To measure the phase shift, we define the output intensity difference operator as

$$\hat{n}_{12}(\phi) = \hat{b}_1^\dagger \hat{b}_1 - \hat{b}_2^\dagger \hat{b}_2 = \cos\phi \left(\hat{a}_2^\dagger \hat{a}_2 - \hat{a}_1^\dagger \hat{a}_1\right) + \sin\phi \left(\hat{a}_1^\dagger \hat{a}_2 + \hat{a}_2^\dagger \hat{a}_1\right) , \tag{3.12}$$

where $\phi = \phi_1 - \phi_2$ is the relative phase shift between the two paths of the interferometer. Since the problem only depends on ϕ, rather than $\phi_{1,2}$ individually, we focus on measuring this relative phase.

One can determine ϕ from the measurement $\langle \hat{n}_{12} \rangle$. However, to achieve an optimal result, the uncertainty associated with this measurement must be minimized. The uncertainty in the measurement of ϕ can be analyzed by developing the variance in $\hat{n}_{12}$ using the error propagation formula via partial derivatives, leading to the following expression:

$$\begin{aligned} \left\langle \hat{n}_{12}^2 \right\rangle - \left\langle \hat{n}_{12} \right\rangle^2 &= \left(\frac{\partial \langle \hat{n}_{12} \rangle}{\partial \phi} \Delta\phi \right)^2 , \\ \Delta\phi &= \frac{\sqrt{\langle \hat{n}_{12}^2 \rangle - \langle \hat{n}_{12} \rangle^2}}{\left| \dfrac{\partial \langle \hat{n}_{12} \rangle}{\partial \phi} \right|} . \end{aligned} \tag{3.13}$$

To show how the uncertainty can be reduced using quantum resources, we consider two different states: a semi-classical state $|\alpha\rangle \otimes |0\rangle = |\alpha, 0\rangle$, corresponding to a coherent state and the vacuum state, and a quantum featured state $|\alpha\rangle \otimes |\xi\rangle = |\alpha, \xi\rangle$, corresponding to a coherent state and a squeezed vacuum state.[2] The main results for these states are presented as follows:

[2]Each mode is related to a specific path

- ► $|\psi_0\rangle = |\alpha, 0\rangle$. In this case, the phase noise is given by

$$\Delta\phi = \frac{1}{|\alpha \sin\phi|} \,. \tag{3.14}$$

This noise is minimized when $\phi = \frac{\pi}{2}$, yielding the minimum noise

$$\Delta\phi_{\text{min}} = \frac{1}{|\alpha|} \,, \tag{3.15}$$

which is the standard quantum limit (SQL), the best precision achievable using only coherent light. For a numeric example, if we evaluate the minimum uncertainty with 25 photons, we obtain

$$\text{SQL}_{2\times 2} = 0.2 \,. \tag{3.16}$$

- ► $|\psi_0\rangle = |\alpha, \xi\rangle$. Now the phase uncertainty is

$$\Delta\phi = \frac{1}{|\alpha|\left(1 - \frac{\sinh^2 r}{|\alpha|^2}\right)} \sqrt{\left(1 + \frac{\sinh^2(2r)}{2|\alpha|^2}\right)\cot^2\phi + \left(\frac{\sinh^2 r}{|\alpha|^2} + \cosh(2r) - \sinh(2r)\cos(\theta - 2\varphi)\right)} \,, \tag{3.17}$$

where $\alpha = |\alpha|e^{i\varphi}$ and $\xi = re^{i\theta}$ ($r > 0$). If we assume the coherent state is strong (large photon number), so that $|\alpha|^2 \gg \sinh^2 r$, then the minimum when $\phi = \frac{\pi}{2}$ and $\varphi = \theta = 0$ is

$$\Delta\phi_{\text{min}} = \frac{e^{-r}}{|\alpha|} \,. \tag{3.18}$$

The accuracy is improved by a factor of e^{-r} respect to the SQL, due to the presence of squeezed light. This expression provides an approximation for strong coherent light, but to evaluate numerically we use the result in Eq. (3.17). For 25 photons, the minimum uncertainty achievable is $2\times 2 = 0.092$ with a squeezing parameter of $|\xi| = 1.17$. While this provides better precision, instead we use a squeezing parameter of 0.576 (the achievable in our laboratory, corresponding to a squeezing degree of -5 dB), which gives an uncertainty of

$$(2\times 2)_\xi = 0.117\,. \tag{3.19}$$

We can clearly observe the advantage of using squeezed light. The next step is to apply the concepts introduced in Section 3.1 to more complex scenarios, where we can measure multiple parameters more efficiently. Results based on this approach are presented in Chapter 5.

3.2. Multi-Port Beam Splitter

In this section, we extend the two-port beam splitter to a multi-port beam splitter (MBS). First, in Section 3.2.1, we discuss the constraints and present the mathematical description of a MBS. Then, in Section 3.2.2, we briefly explain the technique to experimentally implement a MBS in MCFs.

3.2.1. Mathematical description of a Multi-Port Beam Splitter

In the general case, the BS transformation is analogous to Eq. (3.1), where energy conservation must hold, or equivalently, the transformation must be unitary. For 2-port and 3-port BS, restrictions arising from energy conservation determine the transformation coefficients up to phase shifts at the input and output, leading to only one equivalence class to describe the BS. This means that the physical meaning of the transformation remains unchanged when accounting for these phase shifts.

However, for 4-port and higher multi-port BS (MBS), energy conservation does not completely determine all the internal phases of the transformation, leading to a continuous set of different equivalence classes [44]. Consequently, one cannot simply apply phase shifts at the input and output to obtain all possible transformations. The **most general beam splitter** transformations, up to phase shifts at the input or output and assuming equal transmission coefficient's moduli, for 3-port and 4-port systems are given by:

$$B_3 = \frac{1}{\sqrt{3}} \begin{pmatrix} 1 & 1 & 1 \\ 1 & e^{2i\pi/3} & e^{4i\pi/3} \\ 1 & e^{4i\pi/3} & e^{2i\pi/3} \end{pmatrix} , \tag{3.20}$$

$$B_4 = \frac{1}{2} \begin{pmatrix} 1 & 1 & 1 & 1 \\ 1 & e^{i\phi} & -1 & -e^{i\phi} \\ 1 & -1 & 1 & -1 \\ 1 & -e^{i\phi} & -1 & e^{i\phi} \end{pmatrix} . \tag{3.21}$$

The B_3 transformation (and the 2-port case as well, Eq. (3.5)), are in fact the **most general unitary** transformations. For the 4-port case, it may be possible that a unitary transformation that does not represent a beam splitter exists, so we do not claim the former in this case.

For the 3-port BS (and the 2-port case as well, Eq. (3.5)), the transformation represents a Quantum Fourier Transform (QFT), with no free phases. For the 4-port BS, however, there are physically distinct transformations for each value of ϕ, which goes from 0 to π. For $\phi = 0, 1$, we recover a real Hadamard transformation up to row swaps, and for $\phi = \frac{\pi}{2}$, the transformation turns out to be the corresponding QFT in 4-D. Since we have recovered the QFT, we can also perform the DFT (classical case) and inverse QFT. In general and up to a scalar ponderation, B_4 corresponds to a complex Hadamard matrix [45].

Our approach to realizing the transformation in Eq. (3.21) is further elaborated in Chapter 4, where we present a method to implement these transformations with physical systems.

3.2.2. Experimental Implementation of a MBS in MCF

As discussed in Section 3.1, beam splitters can be thought of as coupled waveguide arrays at the correct propagation distance. This approach has been utilized to fabricate balanced optical splitters [46]. Since the core of an optical fiber is essentially a waveguide, an inline beam splitter can be modeled as a coupled waveguide array.

However, in a MCF, each core propagates a signal independently without mutual interference. To implement a MBS, a section of the fiber is tapered, enabling core coupling through strong evanescent effects. This technique is depicted in Fig. 3.4.

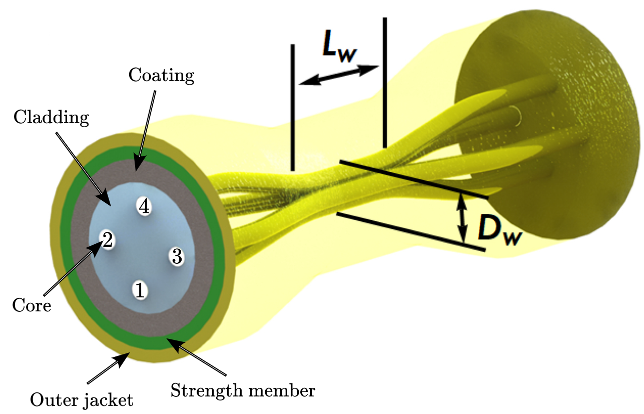

Fig. 3.4: Schematic of a MBS. The fiber is heated along a length L and pulled symmetrically from both ends, stretching and thinning the fiber. The final device is the MBS and has a length L_W and a diameter D_W. Figure from [1].

This tapering technique was recently introduced in [47] and utilized for, e.g., quantum information processing [1], generating multidimensional entanglement [48], and maximizing quantum discord [49]. It is worth noting that, implemented as in [1], the resulting device effectively applies the transformation in Eq. (3.21) when $\phi = 0$.

In Chapter 4, we explore the propagation of quantum light through coupled waveguides, analyzing how this approach enables the implementation of a multi-port beam splitter and its potential applications in quantum optics and information processing.

3.3. Polarization Manipulation in an Optical Fiber

In Section 3.1, we considered interferometry under the assumption that all the light was equally polarized, which allowed for effective interference. Polarization changes and/or fluctuations degrade the quality of the interference, which leads to lower precision in metrology [26], gate errors in photonic quantum computation [27], or increased bit error rate in quantum cryptography [28]. Thus, to apply the concepts discussed in that section, it is crucial to manipulate the polarization. This is not only necessary for interference purposes but also useful for other applications of polarization control, as will be further explored in Section 1.2.

While there are many polarization controllers available, we focus on the Thorlabs inline polarization controller (IPC), shown in Fig. 3.5, as we are working with optical fibers. The IPC is essentially a fiber squeezer, where the magnitude of the applied force is regulated by a screw. The direction of the applied force can be changed by rotating the fiber chamber (without rotating the fiber itself). When the fiber is compressed, the IPC induces stress in the fiber, leading to birefringence in the fiber core, which alters the relative phase between orthogonal polarizations.

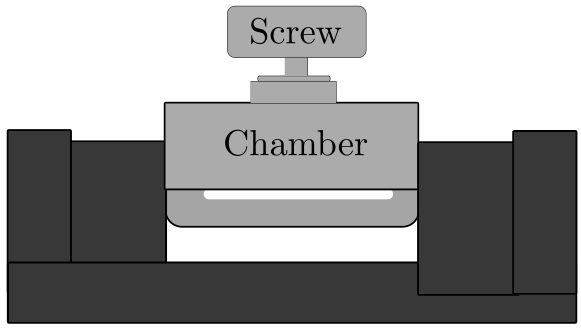

Fig. 3.5: Side view of the inline polarization controller (IPC) by Thorlabs.

To represent the action of the IPC mathematically, consider the case where a force is applied in the vertical direction. The corresponding transformation for the polarization state is given by

$$P(0) = \begin{pmatrix} e^{i\phi_h} & 0 \\ 0 & e^{i\phi_v} \end{pmatrix} , \tag{3.22}$$

acting on the $|H\rangle$ and $|V\rangle$ basis. Here, ϕ_h and ϕ_v are phase shifts applied to the horizontal and vertical polarizations, respectively, depending on the number of turns of the screw. When the applied force forms an angle θ with the vertical direction, we apply a rotation to the operator in Eq. (3.22):

$$P(\theta) = \begin{pmatrix} e^{i\phi_h}\cos^2\theta + e^{i\phi_v}\sin^2\theta & -\left(\sin\theta\cos\theta\left(e^{i\phi_h} - e^{i\phi_v}\right)\right) \\ -\left(\sin\theta\cos\theta\left(e^{i\phi_h} - e^{i\phi_v}\right)\right) & e^{i\phi_h}\sin^2\theta + e^{i\phi_v}\cos^2\theta \end{pmatrix} . \tag{3.23}$$

This transformation gives the action of the IPC in terms of the phases it applies to the horizontal and vertical polarizations. However, in practice, we need the transformation in terms of the number of turns of the screw. To characterize this, let us assume that the polarization state traveling through the fiber is

$$|\psi_0\rangle = p_h|H\rangle + p_v|V\rangle = \begin{pmatrix} p_h \\ p_v \end{pmatrix} , \tag{3.24}$$

and that the polarization state after the action of the IPC is obtained by applying the transformation in Eq. (3.23):

$$|\psi\rangle = P(\theta)|\psi_0\rangle \,. \tag{3.25}$$

For instance, let us evaluate the Bloch parameters (see Section 2.2.2) of the resulting state in Eq. (3.25), as a function of the relative phase $\Delta = \phi_v - \phi_h$, induced when a vertical force ($\theta = 0$) is applied to all the polarization states considered in Section 2.2.2. The obtained results are:

$$\vec{a}_\psi = \begin{cases} (1,0,0)\,, & \text{when } |\psi_0\rangle = |H\rangle, \\ (0,\cos\Delta,\sin\Delta)\,, & \text{when } |\psi_0\rangle = |D^+\rangle, \\ (-1,0,0)\,, & \text{when } |\psi_0\rangle = |V\rangle, \\ (0,-\cos\Delta,-\sin\Delta)\,, & \text{when } |\psi_0\rangle = |D^-\rangle, \\ (0,-\sin\Delta,\cos\Delta)\,, & \text{when } |\psi_0\rangle = |R\rangle, \\ (0,\sin\Delta,-\cos\Delta)\,, & \text{when } |\psi_0\rangle = |L\rangle. \end{cases} \tag{3.26}$$

Each of these is a curve in the Bloch sphere parameterized by Δ (see Fig. 6.4). To determine the dependence on the number of turns, we must know how Δ varies with the number of turns. From Eq. (3.26), it is evident that no information about Δ can be extracted when $|\psi_0\rangle \in |\{H\rangle, |V\rangle\}$. In general, this limitation holds if the force is parallel or orthogonal to the polarization. For other polarizations, one Bloch parameter remains constant—the parameter associated with horizontal and vertical polarization. In practice, this parameter will liketly not remain perfectly constant due to experimental deviations. To address this, we introduce an "error" phase ε, which accounts for variations in the constant Bloch parameter and preserves the Bloch vector's unitarity. Incorporating ε, the Bloch vectors of Eq. (3.26) become

$$\vec{a}_\psi = \begin{cases} (\sin\varepsilon, \cos\varepsilon\cos\Delta, \cos\varepsilon\sin\Delta)\,, & \text{when } |\psi_0\rangle = |D^+\rangle, \\ (\sin\varepsilon, -\cos\varepsilon\cos\Delta, -\cos\varepsilon\sin\Delta)\,, & \text{when } |\psi_0\rangle = |D^-\rangle, \\ (\sin\varepsilon, -\cos\varepsilon\sin\Delta, \cos\varepsilon\cos\Delta)\,, & \text{when } |\psi_0\rangle = |R\rangle, \\ (\sin\varepsilon, \cos\varepsilon\sin\Delta, -\cos\varepsilon\cos\Delta)\,, & \text{when } |\psi_0\rangle = |L\rangle. \end{cases} \tag{3.27}$$

Given the Bloch vector, we can solve for ε from a_1, and then retrieve Δ from a_2 or a_3 (since the Bloch vector is unitary, the Δ value retrieved from a_2 and a_3 will be equal).

The transformation in Eq. (3.23) assumes an ideal case where the fiber core is perfectly aligned with the applied force, such as in a single mode fiber (SMF). For multi-core fibers (MCF), however, the transformation could be more complex due to misalignments between the cores and the applied force, and the fiber's structure influencing the polarization's response depending on the core's location. Thus, for a MCF, there should be a transformation $P_j(\theta)$ for each core. Results towards the reconstruction of these operators are presented in Chapter 6.

Chapter 4

Multi-Port Beam Splitter

In this Chapter, we consider coupled waveguide arrays to model beam splitters, and analytically study light propagation with distinct objectives. First, in Section 4.1, we propagate squeezed states through an optical dimer to better understand squeezed light dynamics, placing special emphasis on a potential squeezing degree conservation. Finally, in Section 4.2, we focus on the capability of MBSs to perform operations by analyzing a four-waveguide array to model a 4-port BS, as it would be on a multi-core fiber, retrieving the general transformation in Eq. (3.21).

4.1. Squeezing Degree Conservation in an Optical Dimer

Propagation through a closed waveguide array system is periodic, making it natural to consider conserved quantities. In this thesis, we investigate the evolution of complex squeezing parameters in an optical dimer, to better understand the dynamics of squeezing propagation by focusing on conserved quantities. Recent work has used this approach to analytically construct multi-mode squeezed states from single-mode squeezed states [25]. However, the perspective of conserved quantities is yet to be explored.

For this purpose, we use the evolution operator of Eq. (3.8). Suppose we inject a single-mode squeezed state into each waveguide, generated as $|\psi_0\rangle = \hat{S}_1(\xi_1)\hat{S}_2(\xi_2)|0\rangle$. After propagating through the dimer, the state evolves into [25]

$$\begin{aligned}|\psi\rangle &= \hat{U}_2(\gamma)\hat{S}_1(\xi_1)\hat{S}_2(\xi_2)\hat{U}_2^{-1}(\gamma)|0\rangle \\ &= \exp\left(\frac{1}{2}\left(T_1^*\hat{a}_1^2 + T_2^*\hat{a}_2 + T_{12}\hat{a}_1^\dagger\hat{a}_2^\dagger - H.c.\right)\right)|0\rangle\,,\end{aligned} \tag{4.1}$$

where $T_{1,2}$ and T_{12} are the complex squeezing parameters of single- and two-mode squeezing, respectively. These parameters can be evaluated using the BCH, arriving at:

$$\begin{aligned}T_1 &= \xi_1 - \left(\xi_1 - e^{2i\delta}\xi_2\right)\sin^2\theta\,, \\ T_2 &= \xi_2 + e^{-2i\delta}\left(\xi_1 - e^{2i\delta}\xi_2\right)\sin^2\theta\,, \\ T_{12} &= -e^{-i\delta}\left(\xi_1 - e^{2i\delta}\xi_2\right)\sin(2\theta)\,.\end{aligned} \tag{4.2}$$

We observe the repetition of the term $\xi_1 - e^{2i\delta}\xi_2$, which dictates the direction and magnitude of changes in the complex squeezing parameters. Notably, when this term equals zero, the propagated state remains unchanged at all points of the propagation. Additionally, T_{12} can be expressed in terms of T_1 and T_2 as

$$T_{12} = e^{-i\delta}\frac{dT_1}{d\theta} = -e^{i\delta}\frac{dT_2}{d\theta}\,. \tag{4.3}$$

This indicates that multi-mode squeezing is maximized when single-mode squeezing varies rapidly.

Regarding conserved quantities, based on the coefficients in Eqs. (4.2), we define

$$\Lambda_1(\delta) = T_1 + e^{2i\delta} T_2 \,, \tag{4.4}$$

$$\Lambda_2(\delta) = \left|T_1 - e^{2i\delta} T_2\right|^2 + |T_{12}|^2 \,, \tag{4.5}$$

which are both constant with respect to θ. Note that the right-hand side of Eq. (4.3) is obtained by differentiating Eq. (4.4). These constants evaluate to

$$\Lambda_1(\delta) = \xi_1 + e^{2i\delta} \xi_2 \,, \tag{4.6}$$

$$\Lambda_2(\delta) = |\xi_1|^2 + |\xi_2|^2 - 2\Re\left(e^{2i\delta} \xi_1^* \xi_2\right) \,. \tag{4.7}$$

Since both Λ_1 and Λ_2 are constants, any combination of them is also a constant. Thus, we define

$$\Lambda_3 = |\Lambda_1(\delta)|^2 + \Lambda_2(\delta) = 2\left(|\xi_1|^2 + |\xi_2|^2\right) \,, \tag{4.8}$$

a third constant that depends solely on the squeezing parameters, $|\xi_1|$ and $|\xi_2|$.

These results reveal key aspects of squeezing dynamics in an optical dimer, offering a deeper understanding of the interplay between single- and two-mode squeezing dynamics, and how initial complex squeezing parameters govern the evolution and stability of the quantum state. Future work will explore extending these results to larger waveguide systems, with particular attention to Eq. (4.3) and the conserved quantities Λ_i. These findings hold potential applications in quantum information processing and sensing, providing a foundation for developing state engineering. A manuscript is currently being prepared.

4.2. Fourier Transform in a 4-Port Beam Splitter with Diagonal Coupling

As mentioned in Section 3.2.2, the tapering technique implements the specific case of Eq. (3.21) when $\phi = 0$. This could be considered a limitation recalling that for $\phi = \frac{\pi}{2}$ a Fourier transform is recovered. In this thesis, we propose varying the diagonal coupling in order to completely parameterize Eq. (3.21). Previous work with a similar approach found applications in quantum light manipulation [43]. However, the effects of varying the relative coupling strengths were not explored.

Consider the system in Fig. 4.1 to modelate the 4-port BS.

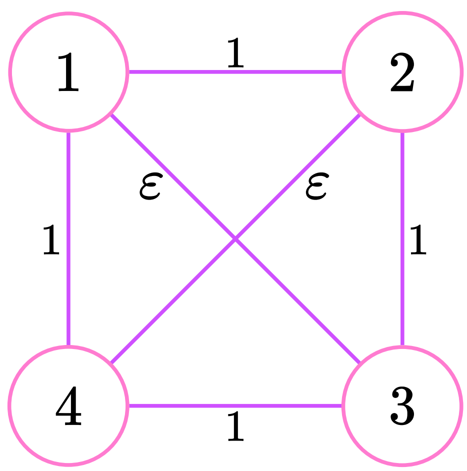

Fig. 4.1: System of 4 coupled waveguides with diagonal coupling. The waveguides, or cores in a MCF, are numbered. 1 and ε are relative coupling strengths, where $\varepsilon \in [0, 1]$.

The system in Fig. 4.1 takes into account that diagonal coupling should be less intense, but the phase acquired through the diagonal is the same as the other sides. The parameter ε represents the fraction that the diagonal coupling is to the sides coupling. The unitary operator that represents this system is

$$U_\varepsilon(\theta;\varepsilon) = \exp\left(i\theta\left(\lambda_{12}+\lambda_{23}+\lambda_{34}+\lambda_{14}+\varepsilon(\lambda_{13}+\lambda_{24})\right)\right)\ , \tag{4.9}$$

where $\lambda_{ij} = \hat{a}_i\hat{a}_j^\dagger + \hat{a}_i^\dagger\hat{a}_j$ and we chose the coupling phase to be $\delta = \frac{\pi}{2}$. Evolving the annihilation operators as $\hat{b}_i = U_\varepsilon^\dagger \hat{a}_i U_\varepsilon$ we find that Eq. (4.9) is equivalent to

$$U_\varepsilon\left(\frac{\pi}{4};\varepsilon\right) = \frac{1}{2}\begin{pmatrix} e^{-\frac{i\pi\varepsilon}{4}} & ie^{\frac{i\pi\varepsilon}{4}} & -e^{-\frac{i\pi\varepsilon}{4}} & ie^{\frac{i\pi\varepsilon}{4}} \\ ie^{\frac{i\pi\varepsilon}{4}} & e^{-\frac{i\pi\varepsilon}{4}} & ie^{\frac{i\pi\varepsilon}{4}} & -e^{-\frac{i\pi\varepsilon}{4}} \\ -e^{-\frac{i\pi\varepsilon}{4}} & ie^{\frac{i\pi\varepsilon}{4}} & e^{-\frac{i\pi\varepsilon}{4}} & ie^{\frac{i\pi\varepsilon}{4}} \\ ie^{\frac{i\pi\varepsilon}{4}} & -e^{-\frac{i\pi\varepsilon}{4}} & ie^{\frac{i\pi\varepsilon}{4}} & e^{-\frac{i\pi\varepsilon}{4}} \end{pmatrix}.$$

To find the real-bordered transformation we consider the following phase shifts at input (D_1) and output (D_2):

$$D_1 = \begin{pmatrix} 1 & 0 & 0 & 0 \\ 0 & e^{\frac{i\pi}{2}(3-\varepsilon)} & 0 & 0 \\ 0 & 0 & -1 & 0 \\ 0 & 0 & 0 & e^{\frac{i\pi}{2}(3-\varepsilon)} \end{pmatrix}, \quad D_2 = \begin{pmatrix} e^{\frac{i\pi}{4}(\varepsilon-8)} & 0 & 0 & 0 \\ 0 & e^{-\frac{i\pi}{4}(2+\varepsilon)} & 0 & 0 \\ 0 & 0 & e^{\frac{i\pi}{4}(\varepsilon-4)} & 0 \\ 0 & 0 & 0 & e^{-\frac{i\pi}{2}(2+\varepsilon)} \end{pmatrix}.$$

Thus, the real-bordered transformation is

$$D_1 U_\varepsilon\left(\frac{\pi}{4};\varepsilon\right) D_2 = \frac{1}{2}\begin{pmatrix} 1 & 1 & 1 & 1 \\ 1 & -e^{-i\pi\varepsilon} & -1 & e^{-i\pi\varepsilon} \\ 1 & -1 & 1 & -1 \\ 1 & e^{-i\pi\varepsilon} & -1 & -e^{-i\pi\varepsilon} \end{pmatrix}, \tag{4.10}$$

which is the quantum Fourier transform (QFT) for $\varepsilon = \frac{1}{2}$. If we compare this expression to Eq. (3.21), we note a few sign changes, nontheless the actual coefficient values over the ϕ and ε domain are exactly the same, so we recover the general complex Hadamard matrix. **It should be possible then to generate any 4-D unitary transformation with the system of Fig. 4.1, adjusting the size of the square** (thus changing the diagonal coupling respect to the sides coupling).

These results highlight the flexibility of the proposed 4×4 **MBS model with diagonal coupling, demonstrating its capability to perform arbitrary 4-D unitary transformations by tuning the relative coupling strengths. Notably, the system is able to perform a QFT, which holds significant applications in quantum information processing and communication, as discussed in Section 1.2.** Future work could explore the experimental realization of such systems and their extension to higher-dimensional transformations.

Chapter 5

Multi-Port Mach-Zehnder Interferometer

In this Chapter, we analytically study a MZI of N inputs and N outputs, labeled as $N \times N$ MZI, in a search for configurations that allows us to make efficient and precise measurements. To this date, we have been working for $N = 3, 4$, although the results appear to extend to higher dimension. We will explore this after the results of this thesis are published.

First, in Section 5.1, we show the mathematical model for the $N \times N$ MZI, and define the maximal uncertainties $\Delta_M \phi$ we will be minimizing. In Section 5.2, we discuss the impact of using a certain set of relative phases (or parameters) to describe the system, and the physical meaning of this free of choice. Sections 5.3 and 5.4 are devoted to numerical results: in Section 5.3 we measure the "same" operator as in the 2×2 case, finding configurations that allow for multi-parameter estimation with enhanced precision due to the presence of squeezed states, and in Section 5.4 we measure an extended operator, obtaining (with coherent light) configurations robust to unwanted phase shifts, and further increasing the precision by utilizing squeezed states.

5.1. Mathematical Model of $N \times N$ MZI

To construct an N×N MZI, the procedure is the same as in the 2×2 case described in Section 3.1.2, but now we use N states or signals for the N paths, along with a N-port BS from Section 3.2.1. Since in our approach we transform the annihilation operators for each path or mode, the N× MZI is represented by Fig. 5.1.

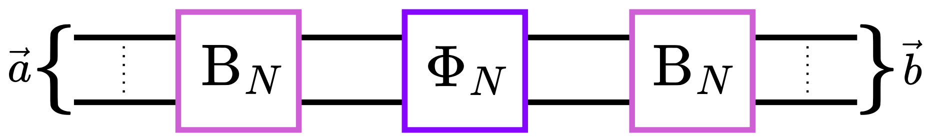

Fig. 5.1: Scheme of an $N \times N$ MZI. $\vec{a}$ and $\vec{b}$ are the vectors containing the annihilation operators at the input and output respectively.

Naming the operator representing the full interferometer as M_N, we have

$$\vec{b} = \mathrm{B}_N \Phi_N \mathrm{B}_N \vec{a} = \mathrm{M}_N \vec{a}\,, \tag{5.1}$$

$$\mathrm{B}_N \equiv \text{Unitary } N \times N \text{ matrix; } \Phi_N = \mathrm{diag}\{e^{i\phi_1}, \ldots, e^{i\phi_N}\}\,.$$

Let us assume we measure $\langle \hat{O} \rangle = \langle \hat{O}(\vec{b}) \rangle$. From this measurement, we should be able to solve for Φ_N. However, in this study, we focus solely on the precision of the measurements performed.

To quantify this, we use the error propagation formula via partial derivatives (as in Eq. (3.13)) to define the maximal uncertainties as

$$\Delta_M \phi_i = \frac{\sqrt{\langle \hat{O}^2 \rangle - \langle \hat{O} \rangle^2}}{\left| \dfrac{\partial \langle \hat{O} \rangle}{\partial \phi_i} \right|}\,. \tag{5.2}$$

Eq. (5.2) represents the noise on ϕ_i when treated as the sole variable in the system. Considering error propagation for $\langle \hat{O} \rangle$, we derive the constraint

$$\sum_{i=1}^{N-1} \left(\frac{\Delta \phi_i}{\Delta_M \phi_i} \right)^2 = 1 \,. \tag{5.3}$$

Eq. (5.2) defines the error ellipse with semi-axes $\Delta_M \phi_i$. Clearly $\Delta \phi_i \leq \Delta_M \phi_i$, putting an upper bound on the uncertainty, that is easy to compute. Thus, minimizing these maximal noises provides a practical first approach to optimizing measurement precision.

5.2. Relevant Phase Shifts

The procedure described in the previous section assumes dependence on all N induced phase shifts ϕ_i. However, the global phase of any quantum state is physically meaningless, so there are many Φ_N physically equivalent. As a consequence, our measurements depend only on **relative phase shits**. A common approach at this point is to fix one of the ϕ_i values to zero. For any measurement, this choice does not affect the physical outcomes. However, this approach alters the parameters used to describe the system, and each parameter has an associated sensitivity[1]. Therefore, from the perspective of parameter uncertainty, the choice of which phase is set to zero is not entirely irrelevant. What should we do then? To address this, let us define the transformation from the N induced phases to all the $\binom{N}{2}$ possible induced relative phases as:

[1]This arises because the derivatives in Eq. (5.2) depend on the chosen parameterization.

$$
\begin{aligned}
T : \{\phi_i\} &\longrightarrow \{\phi_{jk} = \phi_j - \phi_k\} \\
\vec{\phi} &\longmapsto \vec{\phi}_{rel}\,.
\end{aligned}
$$

For $N = 4$, this transformation can be expressed in matrix form as:

$$
\begin{pmatrix} \phi_{12} \\ \phi_{13} \\ \phi_{14} \\ \phi_{23} \\ \phi_{24} \\ \phi_{34} \end{pmatrix} = \begin{pmatrix} 1 & -1 & 0 & 0 \\ 1 & 0 & -1 & 0 \\ 1 & 0 & 0 & -1 \\ 0 & 1 & -1 & 0 \\ 0 & 1 & 0 & -1 \\ 0 & 0 & 1 & -1 \end{pmatrix} \begin{pmatrix} \phi_1 \\ \phi_2 \\ \phi_3 \\ \phi_4 \end{pmatrix}\,. \tag{5.4}
$$

Clearly, $\ker T = \mathrm{span}\{(1, \ldots, 1)\}$ for any N. Thus, from the rank-nullity theorem, we find that rank $T = N - 1$, meaning that *we only need $N - 1$ relative phases to completely describe the system*. While this result is expected, it is explicitly demonstrated here.

Furthermore, the number of sets containing linearly independent relative phases—i.e., the number of sets of parameters we could use—is 1 for $N = 2$ (just $\{\phi_{12}\}$), and for $N \geq 3$ it is

$$
\frac{\binom{N}{2}}{(N-1)!} \prod_{i=1}^{N-2} \left(\binom{N}{2} - \binom{i+1}{2} \right)\,. \tag{5.5}
$$

This sequence follows the progression $1, 3, 15, 256, \ldots$, making it computationally prohibitive to explore all possible combinations in high dimensions. Fortunately, noise behavior tends to be similar across certain sets, so it is unnecessary to analyze every combination exhaustively. In this thesis, we present results for just two parameter sets in the 3×3 and 4×4 cases, while briefly commenting on outcomes for other sets.

But what is the physical meaning of choosing one set of relative phases over another? The relative phases in the selected set are the ones we focus on controlling or measuring during the experiment. Since only $N-1$ of these phases are simultaneously relevant, we can concentrate exclusively on these $N-1$ parameters, choosing them conveniently. This choice of convenience depends on our specific aim, as will be demonstrated.

5.3. Enhancing Precision with Squeezed light

In this section, we demonstrate how optimally choosing the parameter set and utilizing squeezed states can enhance precision in multi-parameter estimation within an $N \times N$ MZI for $N = 3, 4$. To achieve this, we compare the maximal phase shifts uncertainty obtained in the multi-port case (the maximal uncertainties from Eq. (5.2)) with the SQL for the standard 2×2 interferometer (Eq. (3.16)) and its reduced noise when using squeezed sates (Eq. (3.19)). The input state will consist of either a coherent state or a vacuum single-mode squeezed state in each path of the interferometer. All evaluations are conducted under the same conditions: a total of 25 photons and a maximum squeezing parameter of 0.576 per squeezed state (our maximum achievable, -5 dB). For this analysis, we measure $\hat{O}_2 = \hat{n}_{12} = \hat{b}_1^\dagger \hat{b}_1 - \hat{b}_2^\dagger \hat{b}_2$ as a first approach to the problem.

5.3.1. 3×3 MZI

In the 3×3 case, as indicated by Eq. (5.5), there are 3 possible sets of parameters. In this section, we present results for the sets $\{\phi_{12}, \phi_{13}\}$ and $\{\phi_{12}, \phi_{23}\}$. Using the assumptions mentioned earlier and the input state $|\psi_0\rangle = |\alpha, \xi_1, \xi_2\rangle$, where $\alpha = 5$, the main results for the 3×3 interferometer are the ones in Fig. 5.2.

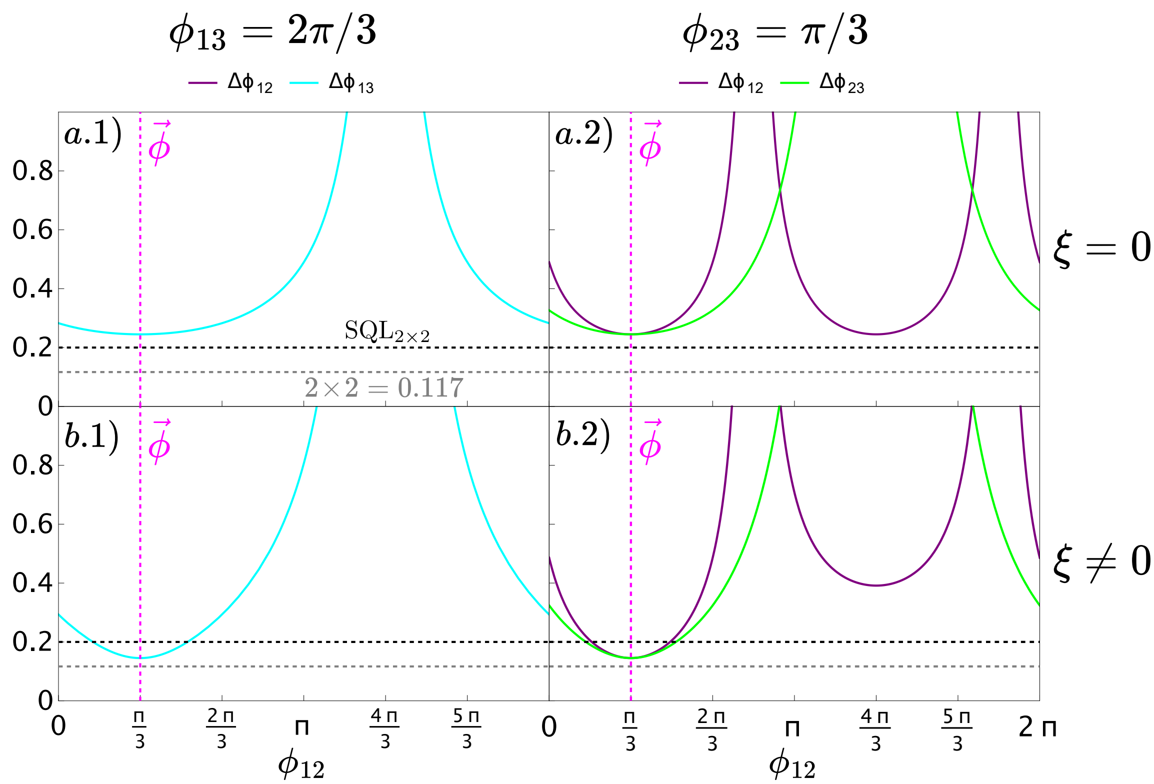

Fig. 5.2: Uncertainty plots for a 3×3 MZI using $\hat{O}_2$ compared with the SQL (back dashed line) and reduced uncertainty (gray dashed line) with $\xi = 0.576$ for the 2×2 MZI. The input state is $|\psi_0\rangle = |\alpha, \xi_1, \xi_2\rangle$ where $\alpha = 5$. The magenta dashed line stands for the same effective Φ_N. Results are shown for two relative phase shift sets, $\{\phi_{12}, \phi_{13}\}$ in a.1) and b.1), and $\{\phi_{12}, \phi_{23}\}$ in a.2) and b.2). Panels a.1) and a.2) correspond to no squeezing ($\xi = 0$), while b.1) and b.2) incorporate squeezing with $\xi_1 = 0.576 \exp\left(\frac{2\pi}{3}i\right)$ and $\xi_2 = 0.576 \exp\left(\frac{4\pi}{3}i\right)$.

In Fig. 5.2, one phase shift is fixed for illustrative purposes. However, the key factor is the specific transformation applied, Φ_N, represented by the magenta dashed line. Let us proceed with the analysis.

Coherent Light (Upper Half of Fig. 5.2)

For coherent light, the achievable uncertainty never equals the SQL of the 2×2 case, regardless of Φ_N or the chosen set of relative phases. This implies that the SQL for the 3×3 MZI is inherently greater than that of the 2×2, specifically:

$$\mathrm{SQL}_{3\times3} = 0.245\,. \tag{5.6}$$

Moreover, the choice of parameter set affects precision. In Fig. 5.2(a.1), for a given Φ_N, only one parameter achieves minimal uncertainty, whereas in Fig. 5.2(a.2), the same Φ_N results in equal minimal uncertainties for both parameters.

Coherent and Squeezed Light (Bottom Half of Fig. 5.2)

Now for the bottom half, we examine the effects of introducing squeezed states into the system by injecting a squeezed state into each of the remaining paths. Comparing Fig. 5.2 (a.1) with (b.1), and (a.2) with (b.2), **we observe a clear improvement in the minimum uncertainty, surpassing both the 2×2 and 3×3 SQLs.** In this case, the uncertainty is[2]

$$(3\times3)_\xi = 0.145\,. \tag{5.7}$$

Interestingly, using only one squeezed state brings the minimum uncertainty close to the $\mathrm{SQL}_{2\times2}$. Adding a second squeezed state further decreases the uncertainty. Again, the choice of parameter set has a significant impact. In Fig. 5.2(b.1), reduced uncertainty is achieved for one parameter, whereas in Fig. 5.2(b.2), two parameters benefit from reduced uncertainty.

This implies that with the parameter set on the left side, increasing the system's dimension does not provide an advantage: only one parameter sees increased uncertainty. Conversely, the parameter set on the right side enables the measurement of two parameters simultaneously with reduced noise, although whether this

[2]If we allow for any squeezing parameter then we achieve uncertainty 0.128 when $|\xi_1| = |\xi_2| = 0.882$.

reduction suffices depends on the specific needs. It is also noteworthy that for the minimum at $\phi_{12} = \frac{4\pi}{3}$ in the right hand side of Fig. 5.2, the uncertainty increases when using squeezed light. This suggests that the advantage of squeezing may be more localized on the system or phase shift parameters space.

5.3.2. 4×4 MZI

In the case of the 4×4 MZI, we have 15 possible sets from Eq. (5.5), and we present results for $\{\phi_{12}, \phi_{13}, \phi_{14}\}$ and $\{\phi_{12}, \phi_{23}, \phi_{34}\}$. Under the same assumptions as before, the input state $|\psi_0\rangle = |\alpha, \xi, 0, 0\rangle$, where $\alpha = 5i$, the main results for the 4×4 MZI are shown in Fig. 5.3.

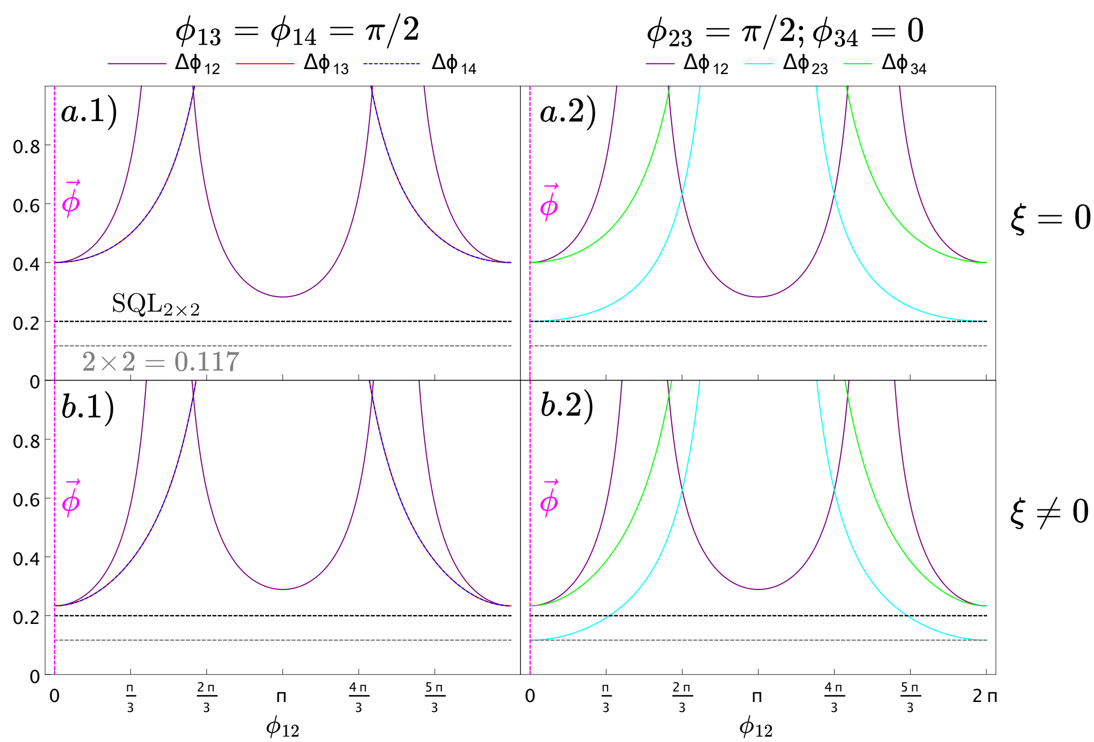

Fig. 5.3: Uncertainty plots for a 4×4 MZI using $\hat{O}_2$ and comparing with the SQL (back dashed line) and reduced noise (gray dashed line) with $\xi = 0.576$ for the standard 2×2 MZI. The input state is $|\psi_0\rangle = |\alpha, \xi, 0, 0\rangle$ where $\alpha = 5i$. The magenta dashed line stands for the same effective Φ_N. Results are presented for two phase shifts sets: $\{\phi_{12}, \phi_{13}, \phi_{14}\}$ for a.1) and b.1), and $\{\phi_{12}, \phi_{23}, \phi_{34}\}$ for a.2) and b.2). Additionally, for a.1) and a.2) we have no squeezing ($\xi = 0$), and for b.1) and b.2), we have a squeezing parameter $\xi = 0.576$.

Coherent Light (Upper Half of Fig. 5.3)

For the 4×4 MZI with coherent light, particularly for the set $\{\phi_{12}, \phi_{23}, \phi_{34}\}$, the minimal uncertainty in one of the phase shifts equals the SQL in 2×2, so this would be the SQL in 4×4 as well:

$$\mathrm{SQL}_{4\times4} = \mathrm{SQL}_{2\times2} = 0.2\,, \tag{5.8}$$

at least for this specific parameter, set, and measurement. This uncertainty level is not achievable for any variable/configuration with, for example, $\{\phi_{12}, \phi_{13}, \phi_{14}\}$. Unlike the 3×3 case, the uncertainty behavior in the 4×4 system is more diverse, with different uncertainty levels depending on the set of relative phases. This makes the choice of phase set even more crucial.

Coherent and Squeezed Light (Bottom Half of Fig. 5.3)

Now, let's turn to the bottom half of Fig. 5.3, where we introduce squeezing. Here, we analyze the results for a system where only one squeezed state is injected. By comparing Fig. 5.3 (a.1) with (a.2), and (a.2) with (b.2), we observe a reduction in uncertainty for the transformation defined by the magenta line in both sets of relative phases. **For every relative phase, except ϕ_{23}, the uncertainty approaches the $\mathrm{SQL}_{3\times3}$, while for the preciser parameter, ϕ_{23}, it approaches $(2\times2)_\xi$.**

It is important to note that we have only presented results with squeezed light applied to one path in the 4×4 case. This is because injecting squeezed states into additional paths does not affect the minimum represented by the magenta line. Instead, the minimum at $\phi_{12} = \pi$ (for both sets) is decreased. However, this reduction is not as significant as the one showed in Fig. 5.3.

5.3.3. Section Conclusions

From the results in the previous subsections, for both the 3×3 and 4×4 MZIs, we can lower the uncertainty below their respective SQLs, achieving reasonable levels for multi-parameter estimation, compared to the 2×2 case. However, in practice, the optimal configuration and even dimension of the system will depend on our specific goals. In the 3×3 case, we can achieve all uncertainties below the $\mathrm{SQL}_{2\times2}$, but only marginally. For the 4×4 case, we can achieve the same precision as in the squeezed-enhanced 2×2 case, but the precision for the other parameters does not go below the $\mathrm{SQL}_{2\times2}$.

Another critical point in the analysis of these results is the apparent impossibility of exploiting multiple squeezed states to simultaneously enhance precision. To better understand this limitation and maximize the utility of squeezed states, further study of squeezing dynamics is required.

5.4. Robust Uncertainty

Up to now, the behavior of uncertainties has been similar to that of the 2×2 interferometer, likely due to the use of the "same" operator, $\hat{O}_2 = \hat{b}_1^\dagger\hat{b}_1 - \hat{b}_2^\dagger\hat{b}_2$. If we naively extend this operator to higher dimensions, we could propose $\hat{O}_3 = \hat{b}_1^\dagger\hat{b}_1 - \hat{b}_2^\dagger\hat{b}_2 + \hat{b}_3^\dagger\hat{b}_3$ and $\hat{O}_4 = \hat{b}_1^\dagger\hat{b}_1 - \hat{b}_2^\dagger\hat{b}_2 + \hat{b}_3^\dagger\hat{b}_3 - \hat{b}_4^\dagger\hat{b}_4$ for 3×3 and 4×4 MZIs, respectively. This approach actively incorporates all the information available at the output.

Naturally, there is a lot of possibilities, such as using any linear combination of the output intensities. Exploring these alternatives could be worthwhile, but as a first approach, we focus on the operators mentioned above. For consistency, we continue using an input state formed in the same manner, with 25 photons and a maximum squeezing parameter of 0.576 when comparing numerical results.

5.4.1. 3×3 MZI

For the 3×3 MZI, we present results using only the set $\{\phi_{12}, \phi_{13}\}$ and coherent light, since for this results the set and dimension do not introduce any useful effect. We propagate two input states composed of coherent light, obtaining the following:

$$\begin{aligned} |\psi_0\rangle &= \left|\alpha_0 e^{i\varphi_1}, 0, \alpha_0 e^{i(\varphi_1+\frac{\pi}{3})}\right\rangle \longrightarrow \frac{\partial \Delta_M \phi_{12}}{\partial \phi_{13}} = 0\,, \\ |\psi_0\rangle &= \left|\alpha_0 e^{i\varphi_1}, 0, \alpha_0 e^{i(\varphi_1-\frac{\pi}{3})}\right\rangle \longrightarrow \frac{\partial \Delta_M \phi_{13}}{\partial \phi_{12}} = 0\,, \end{aligned} \tag{5.9}$$

where $\alpha_0 \in \mathbb{R}_0^+$. From Eq. (5.9), we observe that setting the coherent states' relative phase to $\pm\frac{\pi}{3}$ ensures that the uncertainty of one parameter is independent of the other. This configuration could be beneficial for implementing robust measurements, although only one of the uncertainties can be minimized at a time.

Numerically, the results are less promising. For $\alpha_0 = \frac{5}{\sqrt{2}}$, the minimum of uncertainty achieved is 0.3[3]. Furthermore, introducing squeezed states or using alternative parameter sets does not significantly improve the performance. Squeezed states reduce the uncertainty to approximately 1.8, but only within a narrow parameter regime, and other parameter sets fail to reveal any distinct or advantageous behavior.

5.4.2. 4×4 MZI

In the 4×4 case, we explore the use of squeezed states and additional parameter sets, as the results are notably more promising compared to the 3×3 case.

[3]It is possible to achieve the $\text{SQL}_{3\times 3}$ from the previous section with other configurations.

- $\{\phi_{12}, \phi_{13}, \phi_{14}\}$ For this parameter set, propagating coherent light as $|\psi_0\rangle = |\alpha_1, 0, \alpha_2, 0\rangle$, where $\alpha_{1,2} \in \mathbb{C}$, we find the following results:

$$\frac{\partial \Delta_M \phi_{12}}{\partial \phi_{13}} = \frac{\partial \Delta_M \phi_{14}}{\partial \phi_{13}} = 0\,, \tag{5.10}$$

$$\frac{\partial \Delta_M \phi_{13}}{\partial \phi_{12}} = \frac{\partial \Delta_M \phi_{13}}{\partial \phi_{14}} = 0\,. \tag{5.11}$$

These results are already more promising than those for the 3×3 MZI. First, Eqs. (5.10) and (5.11) hold for any pair of coherent states used. Second, this configuration provides more overall robustness. However, while both Eqs. (5.10) and (5.11) are true simultaneously, $\Delta_M\phi_{12,14}$ and $\Delta_M\phi_{13}$ cannot be minimized at the same time (for the same Φ_N). Consequently, careful tuning of the input states is required, along with a clear understanding of which parameters are being targeted for precise and robust measurements.

Numerically, using $|\alpha_{1,2}| = \frac{5}{\sqrt{2}}$, we achieve an uncertainty of $\mathrm{SQL}_{2\times2} = 0.2$, which is a strong result. When trying to enhance the precision with squeezed states, we find that

$$|\psi_0\rangle = \left|\frac{5}{\sqrt{2}}, -\xi_0, \frac{5}{\sqrt{2}}, -\xi_0\right\rangle \longrightarrow \min \in [0.119, 0.124]\,, \tag{5.12}$$

where $\xi_0 = 0.576$[4]. The resulting uncertainty lies within a small interval due to the squeezed states introducing slight variations related to the previously irrelevant parameters, reducing the robustness achieved. However, this robustness reduction remain small as long as the squeezing parameter is not excessively

[4] Allowing for any squeezing parameter we can achieve a minimum uncertainty of 0.104 with $|\xi_{1,2}| = 0.927$ and $\phi_{12} = \frac{\pi}{2}$

large. This minimum is for either $\phi_{12,14}$ or ϕ_{13}, depending on the chosen parameters for measurement.

- $\{\phi_{12}, \phi_{23}, \phi_{34}\}$ Starting with the same input state $|\psi_0\rangle = |\alpha_1, 0, \alpha_2, 0\rangle$ where $\alpha_{1,2} \in \mathbb{C}$, we find:

$$\frac{\partial \Delta_M \phi_{12}}{\partial \phi_{34}} = \frac{\partial \Delta_M \phi_{34}}{\partial \phi_{12}} = 0\,, \quad \forall \alpha_{1,2}\,, \tag{5.13}$$

$$\partial \Delta_M \phi_{23} = \begin{cases} \dfrac{\partial \Delta_M \phi_{23}}{\partial \phi_{12}}\,, \text{ if } \varphi_1 - \varphi_2 = 0, \\ \dfrac{\partial \Delta_M \phi_{23}}{\partial \phi_{34}}\,, \text{ if } \varphi_1 - \varphi_2 = \pi. \end{cases} \tag{5.14}$$

In this case, not all parameter uncertainties can be minimized or made robust simultaneously, requiring a choice between measuring $\{\phi_{12}, \phi_{23}\}$ or $\{\phi_{34}, \phi_{23}\}$, with the input state adjusted accordingly. For this set, we also achieve $\mathrm{SQL}_{2\times2}$ precision with 25 photons. Further minimizing with squeezed states yields:

$$|\psi_0\rangle = \left|\frac{5}{\sqrt{2}}, -\xi_0, -\frac{5}{\sqrt{2}}, -\xi_0\right\rangle \longrightarrow \min \in [0.119, 0.124]\,, \tag{5.15}$$

where $\xi_0 = 0.576$[5]. The interval for the minimum arises due to the same effect described from Eq. (5.12).

Comparing the results obtained for both sets, we see that numerically, they provide similar precision improvements. However, with $\{\phi_{12}, \phi_{13}, \phi_{14}\}$, one uncertainty can be made independent of two parameters, or two uncertainties can be independent of one parameter each. In contrast, with $\{\phi_{12}, \phi_{23}, \phi_{34}\}$, only two uncertainties can be made independent of a single parameter. The optimal set will thus depend on the specific measurement goals.

[5] Allowing for any squeezing parameter we get the same minimum as with the other parameters set.

5.4.3. Section Conclusions

As presented in this subsection, using $\hat{O}_{3,4}$ introduces more complex behaviors to the measurement, enabling for parameter uncertainties to become independent of other parameters. While the effectiveness in the 3×3 case does not appear particularly promising, the 4×4 case achieves precision levels comparable to the 2×2 interferometer but with added robustness and enhanced precision for certain parameters. This makes the 4×4 configuration a strong candidate for high-precision measurements. Additionally, we have not yet explored a large portion of the 15 parameter sets or input states, leaving room for potentially more interesting results in future studies.

5.5. Chapter Conclusions and Future Work

In this chapter, we have analytically demonstrated that a multi-port MZI can function as an optical sensor for single- or multi-parameter estimation, offering enhanced precision and/or robustness based on specific requirements. Squeezed light enabled precision enhancements for certain parameters, achieving levels comparable to the standard 2×2 MZI. Additionally, measurements involving only coherent light exhibited robustness by flattening uncertainty in targeted parameters, mitigating the influence of unwanted phase variation. Although the precision achieved is not strictly superior to that of the 2×2 interferometer, we expect that the advantages offered by increased dimensionality—such as reduced and/or robust uncertainties—may compensate for this limitation.

These findings present direct applications in quantum metrology and communication, as discussed in Section 1.2. Future work could explore a wider variety of input states and operators measured, as well as pursue experimental verification of the obtained theoretical results.

Chapter 6

Controlling the Polarization in a MCF

As stated in Section 3.3, controlling polarization is essential for successful interferometry. This being the case, this chapter is a necessary first step to experimentally implement the results in previous chapters. In this chapter, we aim to characterize the transformations $P_j(\theta)$, which represent the effective action of the IPC in the j-th core of a 4-core MCF. To achieve this, we apply a force with the IPC in 5 directions to all the polarization states presented in Section 2.2.2 for each core. The data obtained is directly compared with the theoretical SMF model of Section 3.3, and we plan to utilize quantum process tomography to retrieve the transformations directly.

First, in Section 6.1, we describe the experimental setup used in the measurements. Next, in Section 6.2, we present and discuss experimental results gathered for reconstructing these transformations. Finally, in 6.3, we discuss the next steps towards completing the reconstruction process.

6.1. Experimental Setup

To construct the experimental setup, we first show the IPC equipped with a MCF, including our core numeration, in Fig. 6.1.

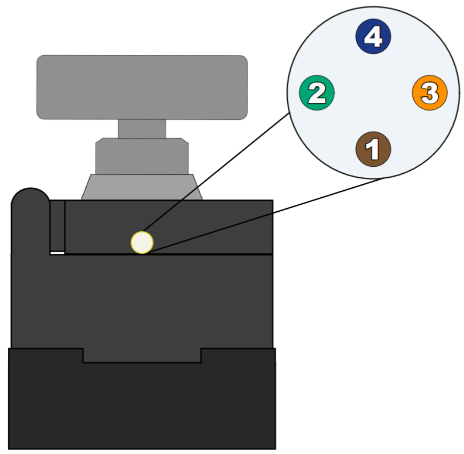

Fig. 6.1: Front view of an IPC with a MCF, with its cores numerated. Figure courtesy of Adheris Contreras, UdeC.

The full setup is represented in Fig. 6.2.

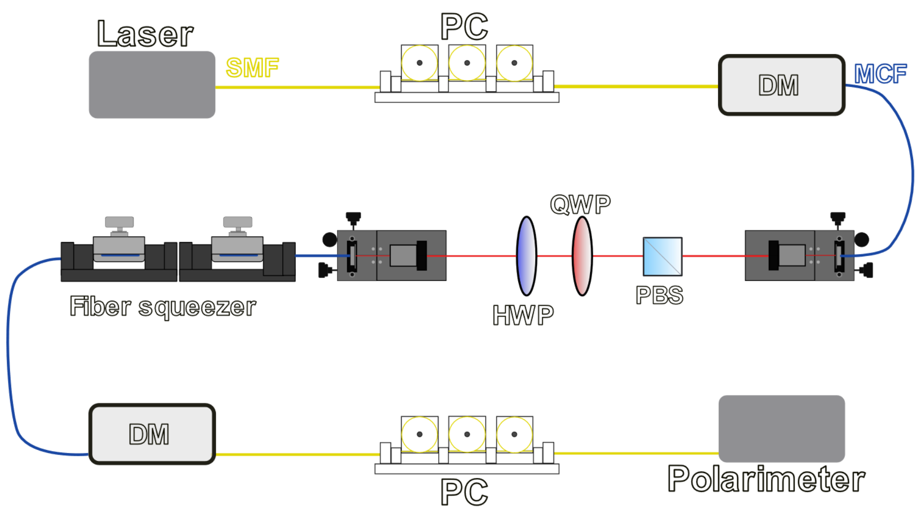

Fig. 6.2: Setup for the characterization of the polarization in MCF. In order of propagation: Laser: continuous wave 1550 nm; PC: polarization controller (for SMF); DM: fiber multiplexer for SMF to MCF; Propagation is now through free space thanks to a launcher; PBS: polarizing beam splitter (we keep the horizontal component); QWP: quarter-wave plate; HWP: half-wave plate; Polarimeter `IPM5300`: takes a SMF and gives the Bloch parameters of the signal. Figure courtesy of Adheris Contreras, UdeC.

The setup operates as follows: The laser signal is first propagated through a SMF. This SMF then passes through the PC, which serves the sole purpose of maximizing the intensity of the signal used. The SMF is subsequently multiplexed into a MCF, with only one core used at a time. The signal is then propagated through free space using a launcher. Afterward, the signal passes through a PBS, retaining only the horizontal component in the path. To maximize the intensity after this step, the first PC is adjusted. The polarization of the signal is then set by adjusting a QWP and a HWP. The adjusted signal is injected back into the corresponding core of the MCF using a launcher. The fiber undergoes squeezing-induced polarization changes through the action of the IPC, which is placed as close as possible to the beginning of the MCF patch-core to minimize internal rotation of the fiber cores. The MCF is demultiplexed again, transferring the signal back to a SMF. This SMF passes through another PC to compensate for any polarization changes that occurred during propagation. Finally, the polarization of the signal is measured using a polarimeter.

The IPM5300-T polarimeter by `Thorlabs` operates using two pairs of Fiber Bragg Gratings (FBGs) with polarization-dependent reflectivity, which divert a small fraction of the transmitted optical power to four detectors. To enable the analysis of an arbitrary polarization state, a quarter-wave fiber plate is positioned between the two FBG pairs, generating the additional polarization states necessary for complete characterization.

6.2. Experimental Polarization Measurements in a MCF

To fully characterize the transformation, we propagate through each core the input states $|H\rangle, |D^+\rangle, |V\rangle, |D^-\rangle, |R\rangle, |L\rangle$. For each combination, the fiber is squeezed in 5 directions corresponding to $\theta = 0, \pm\frac{\pi}{4}, \pm\frac{\pi}{2}$. The directions names are shown in Fig. 6.3.

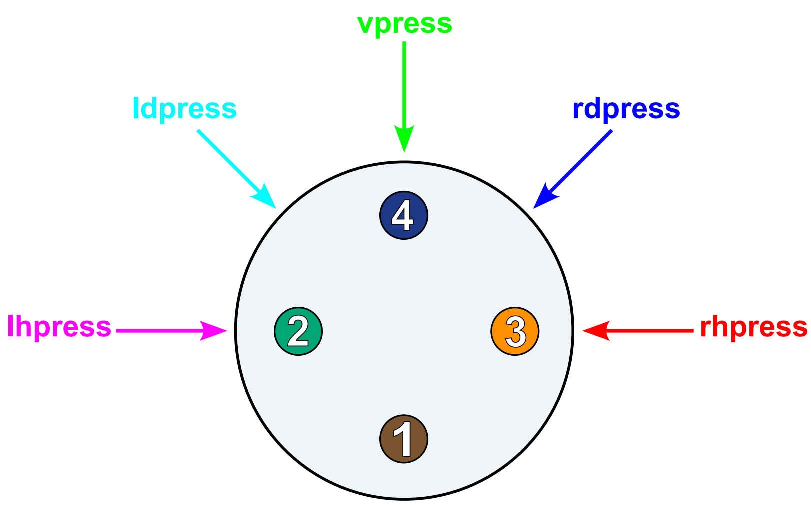

Fig. 6.3: IPC directions nomenclature. The colors are the same as in Fig. 6.4.

The screw is turned at a rate of $\frac{\pi}{8}$ rad every 2 s, starting at turn 10 (when the fiber is held still in the chamber) and stopping at turn 15.5 to avoid permanent deformation.

These results should allow us to reconstruct the IPC transformation on each core for a spacific pressure direction and potentially generalize to other directions.

The results for the 4-th core of the MCF are shown in Fig. 6.4.

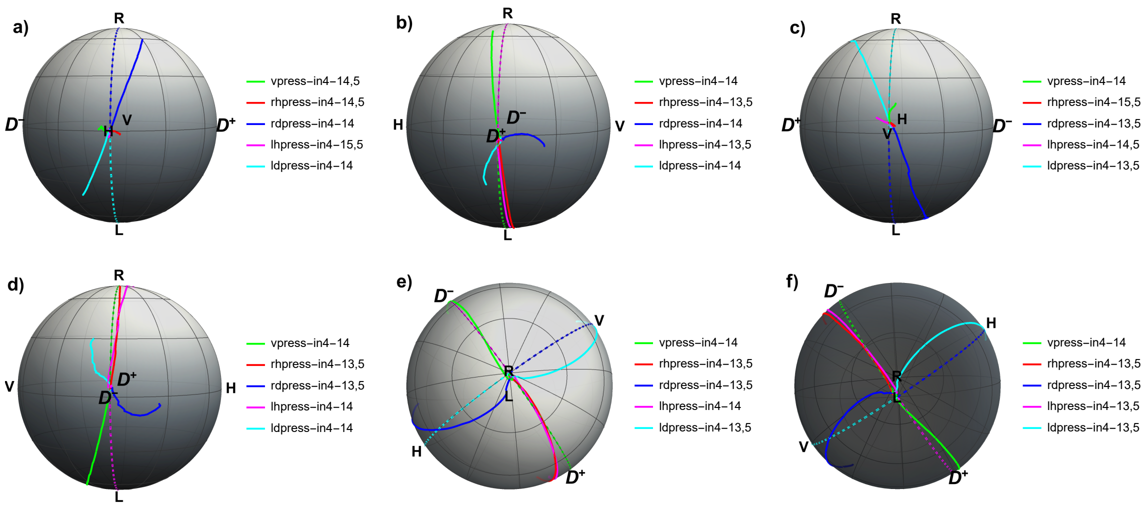

Fig. 6.4: Polarization measurements plots for the 4-th core, for 5 directions and 6 initial states. Figs. a), b), c), d), e) and f) correspond to the input state $|H\rangle$, $|D^{+}\rangle$, $|V\rangle$, $|D^{-}\rangle$, $|R\rangle$ and $|L\rangle$, respectively. The last number of the legends is the turn in which the polarization started to move (the comma is the decimal separator). The segmented lines are the theoretical curves in the case of a SMF. All the curves in this figure are on the front side of the spheres.

From Fig. 6.4, we observe that for the 4-th core, the transformation is similar to that of a central core. Moreover, they differ less in the vertical direction. This is likely because vertical and horizontal forces are much easier to control experimentally. Side cores, such as 2 and 3, show more pronounced deviations due to their positions relative to the applied force, as one would expect. A sense flip between experimental and theoretical curves is evident in some cases, e.g., in Fig. 6.4(b), where vertical and horizontal directions are inverted. Further data and analysis are required to comprehend these discrepancies.

Based on these results, we hypothesize that the corresponding transformation of each core is just the operator on a SMF, but with a different angle for each core. Thus, while the IPC might be aligned at θ, each core will have an associated θ_j. Part of our goal is to test this toy model and discover θ_j.

To evaluate the phase shift dependence on screw turns, we use Eqs. (3.27)—and the analogous for other configurations—to solve for the relative phase Δ and the "error" phase ε. The results obtained for the 4-th core are in Fig. 6.5 (next page).

First, the left half of Fig. 6.5, corresponding to the experimentally retrieved Δ, shows that the maximum Δ is consistently around $\frac{\pi}{2}$. As for the response range, we note that right and left initial polarizations (red and blue lines) exhibit a broader response range, allowing finer control. Initial linear polarizations (other colors) reveal specific force directions that provide enhanced polarization control.

The right half of Fig. 6.5, corresponding to the experimentally retrieved ε, indicates that ε remains relatively small, suggesting that the transformations for the MCF cores are closely resemble those of a SMF. However, ε increases for diagonal forces, likely due to challenges in precise screw alignment. This discrepancy, as well as discrepancies in the Bloch sphere trajectories shown in Fig. 6.4 (c) and (f), could also be explained if the effective angle for the j-th core, θ_j, varies with the force applied. Developing the theoretical formulation of this idea, as well as conducting its experimental verification, is left as a next step for future work.

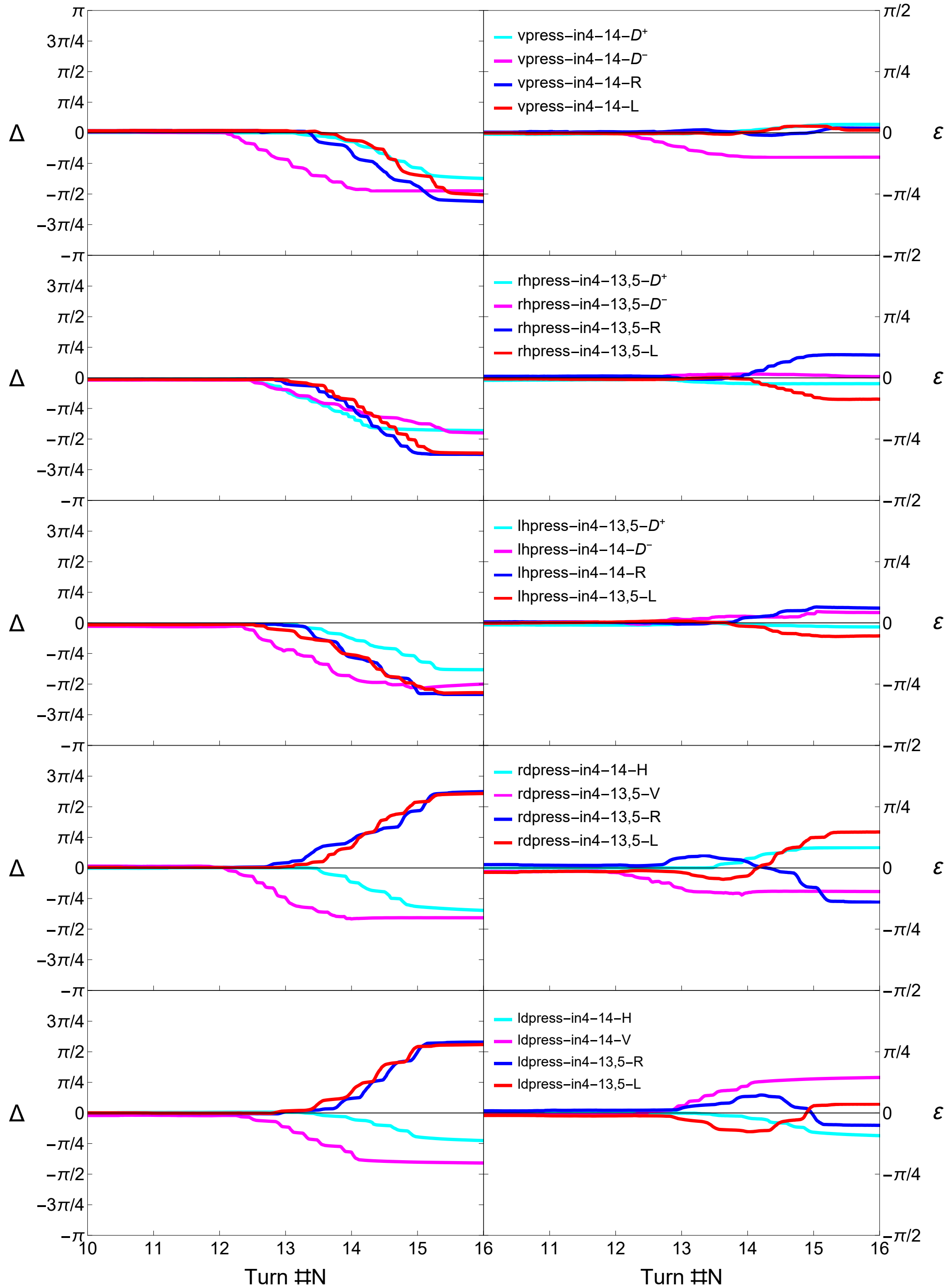

Fig. 6.5: Experimentally retrieved Δ (left-hand side) and ε (right-hand side) for the 4–th core. As seen from the legends, each height level of the figure corresponds to a force direction.

6.3. Future Works

The immediate next steps for this chapter involve completing the characterization of $P_j(\theta)$. As previously mentioned, one approach to improve our toy model would be to consider the displacement of the j-th core relative to the center of the fiber, finding the associated θ_j to each core. Alternatively, quantum process tomography could be performed for each force direction, since we have enough orthonormal basis elements (of the polarization space) to fully characterize the applied process.

Once characterized, the transformations could be applied to MCF interferometry, potentially enabling polarization or phase control in such systems. It is worth noting that simple characterization of the effect of IPCs on MCFs has not yet been reported in the literature.

Developing a simple model for polarization control in MCFs could also be quite relevant for telecommunications, since many opto-electronic devices work for specified polarization modes. In addition, more complicated interferometers involving both spatial and polarization modes could be explored. In such cases, the IPC could enable coupling between these two degrees of freedom.

Chapter 7

Conclusions and Outlook

Multi-core fibers and quantum mechanics have significantly enhanced the capabilities of quantum information, communication and metrology. This thesis has explored integrating MCFs with quantum light to perform unitary transformations, implement precise and/or robust multi-port interferometric sensors, and control polarization within the fiber. These studies highlight the versatility of optical fiber-integrated devices and their potential to address current technological limitations.

In Chapter 4, we studied light propagation through coupled waveguide arrays, given the equivalence between waveguides and optical fiber cores. First, squeezing dynamics in an optical dimer were examined, revealing three conserved quantities over the propagation. These conserved quantities provide insights into the interplay between single- and two-mode squeezing, potentially simplifying quantum state engineering and enabling various applications in quantum computing and information processing. The future of this study relies on a deeper understanding of squeezing dynamics and extending these results to higher dimension.

Later in Chapter 4, we modeled a 4-port beam splitter as a coupled waveguide system with diagonal coupling. It was demonstrated that the relative coupling strengths between side and diagonal couplings completely parameterizes the family of complex Hadamard matrices. Notably, the system is capable of performing a QFT. This makes the device a promising candidate for implementing quantum algorithms and enhancing quantum information processing. Future work should focus on the experimental verification of this result.

In Chapter 5, we explored multi-port MZIs, highlighting the importance of the parameterization choice in adjusting uncertainties, alongside a discussion of the physical meaning. We demonstrated that introducing squeezed light enhances precision beyond the SQL for multi-parameter estimation in both 3×3 and 4×4 MZIs. Additionally, selecting the measured operator allowed for distinct uncertainty behaviors, where certain uncertainties became independent of specific parameters. The achieved precision, specially in the 4×4 interferometer, is comparable to that of standard 2×2 interferometers, with the added advantage of simultaneous estimation of more parameters. These results have direct applications in quantum metrology, improving parameter estimation, and in telecommunications, enhancing capacity and security of information transfer. Future work should explore alternative parameter sets, input states, and measured operator, as well as experimental implementation of these results.

Finally, in Chapter 6, we presented preliminary work on reconstructing the IPC transformations for each core of a 4-core MCF. Our results indicate that the transformations in MCFs are comparable to those in SMFs, as evidenced by similar trayectories on the Bloch sphere. The dependence of the relative phase induced by the IPC on the number of screw turns was modeled by directly appying the theoretical model for a SMF. This data suggests that certain configurations can provide finer control over polarization. Controlling the polarization within the fiber is critical for optimal interferometry and enables applications in quantum information by encoding data in the polarization state. Future efforts should include gathering additional data for statistical analysis, refining the theoretical model, and experimentally verifying polarization controllability. As stated throughout this thesis, controlling polarization is essential for achieving high-quality interference. Consequently, this chapter represents a foundational step towards the experimental integration of MCFs in metrology and the practical implementation of the results in earlier chapters.

References

[1] J. Cariñe, G. Cañas *et al.*, "Multi-core fiber integrated multi-port beam splitters for quantum information processing," *Optica*, vol. 7, no. 5, pp. 542–550, May 2020. https://opg.optica.org/optica/abstract.cfm?uri=optica-7-5-542

[2] D. J. Richardson, J. M. Fini, and L. E. Nelson, "Space-division multiplexing in optical fibres," *Nature Photonics*, vol. 7, no. 5, pp. 354–362, May 2013. https://www.nature.com/articles/nphoton.2013.94

[3] S. Inao, T. Sato *et al.*, "Multicore optical fiber," in *Optical Fiber Communication (1979), paper WB1.* Optica Publishing Group, Mar. 1979, p. WB1. https://opg.optica.org/abstract.cfm?uri=OFC-1979-WB1

[4] K. Saitoh and S. Matsuo, "Multicore Fiber Technology," *Journal of Lightwave Technology*, vol. 34, no. 1, pp. 55–66, Jan. 2016, conference Name: Journal of Lightwave Technology. https://ieeexplore.ieee.org/document/7214203

[5] B. E. Anderson, P. Gupta *et al.*, "Phase sensing beyond the standard quantum limit with a variation on the SU(1,1) interferometer," *Optica*, vol. 4, no. 7, pp. 752–756, Jul. 2017. https://opg.optica.org/optica/abstract.cfm?uri=optica-4-7-752

[6] T. L. S. Collaboration, J. Aasi *et al.*, "Advanced LIGO," *Classical and Quantum Gravity*, vol. 32, no. 7, p. 074001, Mar. 2015. https://dx.doi.org/10.1088/0264-9381/32/7/074001

[7] M. J. Gander, D. Macrae *et al.*, "Two-axis bend measurement using multicore optical fibre," *Optics Communications*, vol. 182, no. 1, pp. 115–121, Aug. 2000. https://www.sciencedirect.com/science/article/pii/S0030401800008178

[8] Y. Ouyang, H. Guo *et al.*, "An In-Fiber Dual Air-Cavity Fabry–Perot Interferometer for Simultaneous Measurement of Strain and Directional Bend," *IEEE Sensors Journal*, vol. 17, no. 11, pp. 3362–3366, Jun. 2017, conference Name: IEEE Sensors Journal. https://ieeexplore.ieee.org/document/7898503

[9] J. Amorebieta, A. Ortega-Gomez *et al.*, "Compact omnidirectional multicore fiber-based vector bending sensor," *Scientific Reports*, vol. 11, no. 1, p. 5989, Mar. 2021. https://www.nature.com/articles/s41598-021-85507-9

[10] Z. Zhao, Z. Liu *et al.*, "Robust in-fiber spatial interferometer using multicore fiber for vibration detection," *Optics Express*, vol. 26, no. 23, pp. 29 629–29 637, Nov. 2018. https://opg.optica.org/oe/abstract.cfm?uri=oe-26-23-29629

[11] L. Yuan, J. Yang *et al.*, "In-fiber integrated Michelson interferometer," *Optics Letters*, vol. 31, no. 18, pp. 2692–2694, Sep. 2006. https://opg.optica.org/ol/abstract.cfm?uri=ol-31-18-2692

[12] J. Villatoro, E. Antonio-Lopez *et al.*, "Interferometer based on strongly coupled multi-core optical fiber for accurate vibration sensing," *Optics Express*, vol. 25, no. 21, pp. 25 734–25 740, Oct. 2017. https://opg.optica.org/oe/abstract.cfm?uri=oe-25-21-25734

[13] J. Amorebieta, A. Ortega-Gomez *et al.*, "Highly sensitive multicore fiber accelerometer for low frequency vibration sensing," *Scientific Reports*, vol. 10, no. 1, p. 16180, Sep. 2020. https://www.nature.com/articles/s41598-020-73178-x

[14] F. Tan, Z. Liu *et al.*, "Stable Torsion Sensor with Tunable Sensitivity and Rotation Direction Discrimination Based on a tapered Trench-Assisted Multi Core Fiber," in *Optical Fiber Communication Conference (2018), paper W1K.6*. Optica Publishing Group, Mar. 2018, p. W1K.6. https://opg.optica.org/abstract.cfm?uri=OFC-2018-W1K.6

[15] H. Zhang, Z. Wu *et al.*, "Directional torsion and temperature discrimination based on a multicore fiber with a helical structure," *Optics Express*, vol. 26, no. 1, pp. 544–551, Jan. 2018. https://opg.optica.org/oe/abstract.cfm?uri=oe-26-1-544

[16] L. Yuan, J. Yang, and Z. Liu, "A Compact Fiber-Optic Flow Velocity Sensor Based on a Twin-Core Fiber Michelson Interferometer," *IEEE Sensors Journal*, vol. 8, no. 7, pp. 1114–1117, Jul. 2008, conference Name: IEEE Sensors Journal. https://ieeexplore.ieee.org/document/4567507

[17] L. Duan, P. Zhang *et al.*, "Heterogeneous all-solid multicore fiber based multipath Michelson interferometer for high temperature sensing," *Optics Express*, vol. 24, no. 18, pp. 20 210–20 218, Sep. 2016. https://opg.optica.org/oe/abstract.cfm?uri=oe-24-18-20210

[18] S. Cheng, W. Hu *et al.*, "Tapered multicore fiber interferometer for ultra-sensitive temperature sensing with thermo-optical materials," *Optics*

Express, vol. 29, no. 22, pp. 35 765–35 775, Oct. 2021. https://opg.optica.org/oe/abstract.cfm?uri=oe-29-22-35765

[19] H. Fu, Q. Wang *et al.*, “Fe2O3 nanotube coating micro-fiber interferometer for ammonia detection,” *Sensors and Actuators B: Chemical*, vol. 303, p. 127186, Jan. 2020. https://www.sciencedirect.com/science/article/pii/S0925400519313851

[20] J.-T. Dong, C.-H. Cheng *et al.*, “Highly sensitive optofluidic refractive index sensor based on a seven-liquid-core Teflon-cladding fiber,” *Optics Express*, vol. 28, no. 18, pp. 26 218–26 227, Aug. 2020. https://opg.optica.org/oe/abstract.cfm?uri=oe-28-18-26218

[21] J. R. Guzmán-Sepúlveda, R. Guzmán-Cabrera *et al.*, “A Highly Sensitive Fiber Optic Sensor Based on Two-Core Fiber for Refractive Index Measurement,” *Sensors*, vol. 13, no. 10, pp. 14 200–14 213, Oct. 2013. https://www.mdpi.com/1424-8220/13/10/14200

[22] C. Gerry and P. Knight, *Introductory Quantum Optics*. Cambridge: Cambridge University Press, 2004. https://www.cambridge.org/core/books/introductory-quantum-optics/B9866F1F40C45936A81D03AF7617CF44

[23] N. Biagi, S. Francesconi *et al.*, “Photon-by-photon quantum light state engineering,” *Progress in Quantum Electronics*, vol. 84, p. 100414, Jun. 2022. https://www.sciencedirect.com/science/article/pii/S0079672722000398

[24] A. M. Lance, H. Jeong *et al.*, “Quantum-state engineering with continuous-variable postselection,” *Physical Review A*, vol. 73, no. 4, p. 041801, Apr. 2006. https://link.aps.org/doi/10.1103/PhysRevA.73.041801

[25] S. Rojas-Rojas, E. Barriga *et al.*, “Manipulation of multimode squeezing in a coupled waveguide array,” *Physical Review A*, vol. 100, no. 2, p. 023841, Aug. 2019. https://link.aps.org/doi/10.1103/PhysRevA.100.023841

[26] E. Polino, M. Valeri *et al.*, “Photonic quantum metrology,” *AVS Quantum Science*, vol. 2, no. 2, p. 024703, Jun. 2020. https://doi.org/10.1116/5.0007577

[27] J. Romero and G. Milburn, “Photonic Quantum Computing,” Apr. 2024, arXiv:2404.03367 [quant-ph]. http://arxiv.org/abs/2404.03367

[28] N. Gisin, G. Ribordy *et al.*, “Quantum cryptography,” *Reviews of Modern Physics*, vol. 74, no. 1, pp. 145–195, Mar. 2002. https://link.aps.org/doi/10.1103/RevModPhys.74.145

[29] S. L. Braunstein and C. M. Caves, “Statistical distance and the geometry of quantum states,” *Physical Review Letters*, vol. 72, no. 22, pp. 3439–3443, May 1994. https://link.aps.org/doi/10.1103/PhysRevLett.72.3439

[30] M. G. A. Paris, “Quantum estimation for quantum technology,” *International Journal of Quantum Information*, vol. 07, no. supp01, pp. 125–137, Jan. 2009. https://www.worldscientific.com/doi/abs/10.1142/S0219749909004839

[31] V. Giovannetti, S. Lloyd, and L. Maccone, “Advances in quantum metrology,” *Nature Photonics*, vol. 5, no. 4, pp. 222–229, Apr. 2011. https://www.nature.com/articles/nphoton.2011.35

[32] V. Giovannetti, S. Lloyd, and L. Maccone, “Quantum-Enhanced Measurements: Beating the Standard Quantum Limit,” *Science*, vol. 306, no. 5700, pp. 1330–1336, Nov. 2004. https://www.science.org/doi/10.1126/science.1104149

[33] J. Miller, L. Barsotti *et al.*, "Prospects for doubling the range of Advanced LIGO," *Physical Review D*, vol. 91, no. 6, p. 062005, Mar. 2015. https://link.aps.org/doi/10.1103/PhysRevD.91.062005

[34] A. Montanaro, "Quantum algorithms: an overview," *npj Quantum Information*, vol. 2, no. 1, pp. 1–8, Jan. 2016. https://www.nature.com/articles/npjqi201523

[35] P. Kok, W. J. Munro *et al.*, "Linear optical quantum computing with photonic qubits," *Reviews of Modern Physics*, vol. 79, no. 1, pp. 135–174, Jan. 2007. https://link.aps.org/doi/10.1103/RevModPhys.79.135

[36] L. Ruiz-Perez and J. C. Garcia-Escartin, "Quantum arithmetic with the quantum Fourier transform," *Quantum Information Processing*, vol. 16, no. 6, p. 152, Apr. 2017. https://doi.org/10.1007/s11128-017-1603-1

[37] M. A. Nielsen and I. L. Chuang, *Quantum Computation and Quantum Information: 10th Anniversary Edition*, Dec. 2010, iSBN: 9780511976667 Publisher: Cambridge University Press. https://www.cambridge.org/highereducation/books/quantum-computation-and-quantum-information/01E10196D0A682A6AEFFEA52D53BE9AE

[38] D. Tong, "Lectures on Quantum Field Theory," University of Cambridge, accessed Jan. 2025. https://www.damtp.cam.ac.uk/user/tong/qft.html

[39] P. A. M. Dirac and N. H. D. Bohr, "The quantum theory of the emission and absorption of radiation," *Proceedings of the Royal Society of London. Series A, Containing Papers of a Mathematical and Physical Character*, vol. 114, no. 767, pp. 243–265, Jan. 1997. https://royalsocietypublishing.org/doi/abs/10.1098/rspa.1927.0039

[40] S. M. Barnett and D. T. Pegg, "Phase in quantum optics," *Journal of Physics A: Mathematical and General*, vol. 19, no. 18, p. 3849, Dec. 1986. https://dx.doi.org/10.1088/0305-4470/19/18/030

[41] M. Uria, P. Solano, and C. Hermann-Avigliano, "Deterministic Generation of Large Fock States," *Physical Review Letters*, vol. 125, no. 9, p. 093603, Aug. 2020. https://link.aps.org/doi/10.1103/PhysRevLett.125.093603

[42] M. Uria, A. Maldonado-Trapp *et al.*, "Emergence of non-Gaussian coherent states through nonlinear interactions," *Physical Review Research*, vol. 5, no. 1, p. 013165, Mar. 2023. https://link.aps.org/doi/10.1103/PhysRevResearch.5.013165

[43] S. Rojas-Rojas, C. Muñoz *et al.*, "Analytic evolution for complex coupled tight-binding models: Applications to quantum light manipulation," *Physical Review Research*, vol. 6, no. 3, p. 033224, Aug. 2024. https://link.aps.org/doi/10.1103/PhysRevResearch.6.033224

[44] H. J. Bernstein, "Must quantum theory assume unrestricted superposition?" *Journal of Mathematical Physics*, vol. 15, no. 10, pp. 1677–1679, Oct. 1974. https://doi.org/10.1063/1.1666523

[45] W. Tadej and K. Życzkowski, "A Concise Guide to Complex Hadamard Matrices," *Open Systems & Information Dynamics*, vol. 13, no. 2, pp. 133–177, Jun. 2006. https://doi.org/10.1007/s11080-006-8220-2

[46] P. Vildoso, R. A. Vicencio, and J. Petrovic, "Ultra-low-loss broadband multiport optical splitters," *Optics Express*, vol. 31, no. 8, pp. 12 703–12 716, Apr. 2023. https://opg.optica.org/oe/abstract.cfm?uri=oe-31-8-12703

[47] L. Gan, R. Wang *et al.*, "Spatial-Division Multiplexed Mach–Zehnder Interferometers in Heterogeneous Multicore Fiber for Multiparameter Measurement," *IEEE Photonics Journal*, vol. 8, no. 1, pp. 1–8, Feb. 2016, conference Name: IEEE Photonics Journal. https://ieeexplore.ieee.org/document/7377003

[48] E. Gómez, S. Gómez *et al.*, "Multidimensional Entanglement Generation with Multicore Optical Fibers," *Physical Review Applied*, vol. 15, no. 3, p. 034024, Mar. 2021. https://link.aps.org/doi/10.1103/PhysRevApplied.15.034024

[49] J. Cariñe, M. N. Asan-Srain *et al.*, "Maximizing quantum discord from interference in multi-port fiber beamsplitters," *npj Quantum Information*, vol. 7, no. 1, pp. 1–8, Dec. 2021. https://www.nature.com/articles/s41534-021-00502-2